Buckling design optimization of tow-steered composite panels and cylindrical shells considering aleatory and epistemic uncertainties

Fina, Marc; Bisagni, Chiara

DOI
10.1007/s00466-024-02589-8

Publication date
2025

Document Version
Final published version

Published in
Computational Mechanics

Citation (APA)
Fina, M., & Bisagni, C. (2025). Buckling design optimization of tow-steered composite panels and cylindrical shells considering aleatory and epistemic uncertainties. *Computational Mechanics*, *76*(1), 59-92. Article 113752. https://doi.org/10.1007/s00466-024-02589-8

Computational Mechanics
https://doi.org/10.1007/s00466-024-02589-8

ORIGINAL PAPER

Buckling design optimization of tow-steered composite panels and cylindrical shells considering aleatory and epistemic uncertainties

Marc Fina[1] · **Chiara Bisagni**[2,3]

Received: 20 May 2024 / Accepted: 19 December 2024

Abstract
Aerospace structures are thin-walled shell structures whose load-bearing capacity is often limited by buckling phenomena. The application of variable angle tow (VAT) composites allows to increase the buckling resistance by tailoring the fiber paths. Fiber placement technologies such as automated fiber placement and continuous tow shearing for VAT composites have been improved enormously in recent years. However, induced material and geometric uncertainties from the manufacturing process have a major influence on the structural performance. The paper focuses on appropriate uncertainty quantification for VAT composites, selecting various uncertainty models based on available data. Different uncertainty models are introduced to quantify the natural variability (aleatory uncertainty) and lack of knowledge (epistemic uncertainty). An uncertain fiber path definition with fuzzy variables is presented to model fiber path deviations. In addition, geometric imperfections are modeled as random fields and as Fourier series to analyze the imperfection sensitivity. Based on this, a design optimization of VAT composites is performed in presence of uncertainties. The introduced methods are demonstrated on a VAT composite panel and a cylindrical shell. Geometric imperfection measurements are provided for the VAT composite cylindrical shell to validate the approach based on experimental results. This paper contributes to a better understanding of uncertainties of tow-steered structures. The results reveal a potential conflict in optimizing the robustness measures (e.g. minimizing the variation of the buckling loads) and enhancing the performance measures (e.g. maximizing the mean value of the buckling loads) visualized by Pareto fronts. This emphasizes the need to consider uncertainties in a design process of VAT composite shells based on multi-objective optimization.

Keywords Buckling analysis · Uncertainty quantification · Variable angle tow composite shells · Geometric imperfections · Monte-Carlo-Simulation · Artificial neural network

1 Introduction

The next generation of commercial aircraft demands advanced materials and designs to become more sustainable. Variable angle tow (VAT) composites have the potential to satisfy these demands of modern aircraft. With spatially varying fiber orientations, the structural performance can be significantly improved. In numerous research papers it is proven that VAT composites can outperform classical composites with tow paths in strength and stiffness [6, 45, 50]. Brooks et al. [9] quantify the improvements by a fuel burn minimization of up to 2.4% and weight reduction of 24% relative to an optimized classical composite wing design.

However, aerospace structures are thin-walled shell structures whose load-bearing capacity is limited by buckling phenomena. In various theoretical and experimental studies, it is demonstrated that the buckling resistance can be increased by tailoring the fiber paths. In [12, 33, 37, 53, 82], possible buckling performance improvements of VAT composites panels are studied. It is well known that thin-walled shell structures are very sensitive to geometric and loading imperfections. An interesting task of VAT compos-

✉ Marc Fina
marc.fina@kit.edu

Chiara Bisagni
chiara.bisagni@polimi.it

[1] Institute for Structural Analysis, Karlsruhe Institute of Technology (KIT), Kaiserstr. 12, 76131 Karlsruhe, Germany

[2] Department of Aerospace Science and Technology, Politecnico di Milano (POLIMI), Via La Masa 34, 20156 Milano, Italy

[3] Faculty of Aerospace Engineering, Delft University of Technology (TU Delft), Kluyverweg 1, 2629 Delft, The Netherlands

Published online: 06 February 2025

ites is the potential to reduce the imperfection sensitivity. In [82], Koiter's asymptotic theory is used to optimize plate-like post-buckling behavior of cylindrical panels under compression loading with respect to the VAT design variables. The results show that the imperfection sensitivity can be effectively eliminated.

Furthermore, numerous research papers explore the impact of tow steering on shell structures. In [63], the influence of radius/length aspect ratio on buckling of cylinders in bending is investigated. White et al. [83] investigate the compression of large-scale VAT composite cylindrical shells. Labans & Bisagni [44] present an experimental and numerical comparison between a classical laminated cylinder and a VAT composite cylinder manufactured by automated fiber placement (AFP). In the context of aircraft fuselage applications, Labans et al. [45] investigate a cylinder with cutouts under bending conditions. Groh & Wu [34] explore the post-buckling behavior of tow-steered shells with cutouts of different sizes manufactured by AFP. They illustrate how structural effects associated with cutouts in tow-steered cylinders can be mitigated.

The AFP manufacturing technology for VAT composites was developed in the 1980s [52]. To reduce process-induced defects, such as fiber wrinkling, the Continuous Tow Shearing (CTS) technique has been developed by [41]. The idea of this method is to eliminate the defects by shearing the tow instead of bending. Lincoln et al. [48] calculated knockdown factors (KDFs) for a CTS cylinder to analyze the design space and quantify the shearing effect on the imperfection sensitivity. In their context, a more imperfection insensitive cylinder means an increase in KDF. They note, if the influence of geometric imperfections on the pre-buckling strain field can be reduced, then the KDF of the cylinder can be significantly increased. It is demonstrated that the KDF of a CTS cylinder under axial compression can be increased by 30%, and the specific buckling load can be 4% higher than that of an optimally designed classical laminated cylinder with a straight fiber laminate. In a subsequent paper by Lincoln et al. [49], a reliability-based optimization using the first-order second-moment (FOSM) method is performed. They calculate buckling loads of an imperfect CTS cylinder taking imperfections from a measured dataset. One of their investigation reveals the possibility of minimizing mass while ensuring a constant thickness-normalized buckling load.

In Brooks et al. [9], two reasons are given why existing aerostructures generally do not fully exploit the advantages offered by tow steering. One reason is the limited work that measures the advantages of tow steering in real-world composite designs, like a wing structure. Another reason is that no one has experience in defining certification standards for tow-steered structures.

To define certification standards a knowledge about uncertainties is essential. Material and geometric uncertainties of VAT composites can arise from different sources. A key role is played by the manufacturing processes. An overview of process-induced defects is given in [1, 2, 38, 50, 51]. According to this literature the main manufacturing failures that have a large influence on the structural performance are variation of fiber orientation, fiber discontinuities, wrinkling, gaps and overlaps. In [85], a perturbation-based stochastic finite element method is applied to investigate the variability in mechanical performance of VAT composite panels. Wang et al. [79] propose a reliability based design optimization approach to consider stochastic variations of the winding angle subject to VAT composite cylinders under axial compression. Pagani et al. [59] model flaws of VAT composite panels via stochastic fields and analyze the stochastic response of fiber and matrix scale stresses affected by multi-scale uncertainty defects. Even though a few works have been found, the authors note a scarcity in the literature addressing uncertainty quantification (UQ) in VAT composites. In particular, no literature is found that incorporates the modeling of both aleatory and epistemic uncertainties.

However, a design of VAT shell structures with deterministic models implies precision. In reality, all data and information are characterized by aleatory and epistemic uncertainty. Aleatory uncertainty is the natural variability and is modeled with random variables. This is already implemented in probabilistic shell design, see, e.g., [43, 46, 55, 75]. Epistemic uncertainty is related to limited knowledge, e.g., incomplete or imprecise data and is modeled with interval and fuzzy variables. How aleatory and epistemic uncertainty can be considered simultaneously is a widely debated topic in research. The different methods are summarized under the terms imprecise probabilities [4, 16] or polymorphic (mixed/hybrid) uncertainties [32]. The idea is to choose the correct uncertainty model (random, interval, fuzzy variables and/or combinations of them) based on the available data. This is intended to ensure a more truthful modeling. In contrast to other approaches, the main idea of the concept of polymorphic uncertainties is the consideration of more than one uncertainty characteristic in one parameter [32]. This approach has been already applied for different engineering problems: seismic performance of buildings [81], scattering material properties of wood [65], modeling of footbridges [25, 69], reinforced concrete bridge design [30] among many others.

In [18, 27–29], the concept is initially introduced for shell buckling problems, where the lack of knowledge in a probabilistic modeling of geometric imperfections of isotropic cylindrical shells is quantified. In detail, the required correlation parameters for a random field approach is developed based on experimental data. The epistemic uncertainty is considered by the definition of the correlation parameters as fuzzy variables. Further studies to the sensitivity analysis and non-Gaussian shell imperfections are presented in [23,

24, 66]. In [22], an optimization approach under polymorphic uncertainties is initially tested on a simple isotropic shell panel. A polymorphic uncertainty quantification for various types of imperfections, such as surface, boundary, material, and thickness imperfections, along with a novel design concept for shells based on a fuzzy-valued safety level, is presented in [26]. The main objective of the mentioned papers is to open up new perspectives moving away from deterministic thinking in shell buckling, which should be further explored for VAT composites.

Compared to classical composites, fiber steering expands the design space. In particular, for real tow-steered structures with a large number of degrees of freedom and multiple layers, an advanced design optimization using computationally efficient algorithms is required. It is not obvious which tow paths results to maximize the buckling performance. However, in addition to the fiber path variables, further design variables and constraints are of interest. For example, Wang et al. [80] present an aeroelastic and local buckling optimization of a full-scale VAT composite wing-box structure. The design variables, including wing-skin thicknesses, fiber paths, and wing-spar geometry, are optimized simultaneously with respect to static failure, aeroelastic, buckling, and manufacturing constraints. In [61], a fiber path formulation is proposed to extend the range of possible fiber paths. The elaborate optimization problem is performed using a neural network combined with a particle swarm optimizer. Rouhi et al. [64] presents a multi-objective optimization method to design VAT composites cylinders subjected to bending. They use radial basis functions surrogate models to approximate the high fidelity FE analysis in the optimization process. Various genetic algorithm optimizations of CTS rocket launch structures are discussed in [47].

In the literature, various methods have been proposed to optimize complex tow-steered structures. This paper focuses on introducing a UQ approach with aleatory and epistemic uncertainty models in buckling design optimization. Therefore, the optimization problem is limited to fiber path parameters as the design variables. However, the proposed approach can also be applied to more complex tow-steered structures with multiple layers and a higher number of degrees of freedom, incorporating design variables such as layer thicknesses and the number of layers. The first part of the paper is to demonstrate an appropriate UQ of fiber orientation angle deviations and shell imperfections based on experimental data. In order to investigate the imperfection sensitivity of a VAT composite panel, geometric imperfections are applied as random fields with different correlation parameters. For different correlated random imperfections, the statistical moments, such as mean and standard deviation, are evaluated. Furthermore, the fiber path is defined with fuzzy variables leading to an uncertain fiber path as a fuzzy function and an uncertain buckling load as a fuzzy output variable. Furthermore, a buckling design optimization of tow-steered composite shells considering aleatory and epistemic uncertainties is presented. Optimizing with uncertain parameters demands the use of a multi-loop algorithm and is computationally expensive. Therefore, a surrogate model strategy is proposed using artificial neural networks. To apply an optimization algorithm, deterministic values are required to evaluate the fitness. For instance, in case of a stochastic output, the mean value and the coefficient of variation are suitable deterministic quantities. In case of a fuzzy valued output, the area or centroid of the fuzzy output variable are quantities to operate an optimization algorithm. Such quantities are also called uncertainty/information reduction measures. In [10, 67], multiple measures are discussed and classified to describe the robustness and performance of a structure. Robustness and performance of a structure can be conflicting in multi-objective optimization tasks. This conflict is illustrated with a Pareto front on the results of a VAT composite panel and cylindrical shell structure.

In particular, the paper presents an approach how to address uncertainties in buckling design optimization. On the way, potential conflicts between robustness and performance optimization objectives are illustrated. Additionally, it is analyzed if VAT composites shells are less sensitive to uncertainties compared to classical composites. The paper aims to initiate a paradigm shift moving away from the classical (deterministic) optimization. It's innovative contributions and key features can be summarized as follows:

- Introduction of aleatory and epistemic uncertainty models for VAT composites shells
- Uncertainty quantification (UQ) of fiber angle deviations and shell imperfections based on experimental data
- Comprehensive study to the imperfection sensitivity of VAT composite panels using random field technique
- Uncertain fiber path definition using fuzzy functions
- Multi-objective design optimization of VAT composite shells considering aleatory and epistemic uncertainties
- Discussion of the robustness and performance of VAT structures in presence of uncertainties based on Pareto fronts
- Surrogate model strategy with artificial neural networks

In Sect. 2, an overview of basic uncertainty models is provided, including the definition of fuzzy and random fields. In Sect. 3, the strategy for performing a multi-objective optimization under uncertainties is presented. Subsequently, Sect. 4 introduces an uncertain fiber path definition using fuzzy functions. The practical application of the concept is illustrated on a VAT composite panel and cylindrical shell in Sect. 5. Finally, Sect. 6 contains a summary of conclusions and possible future studies.

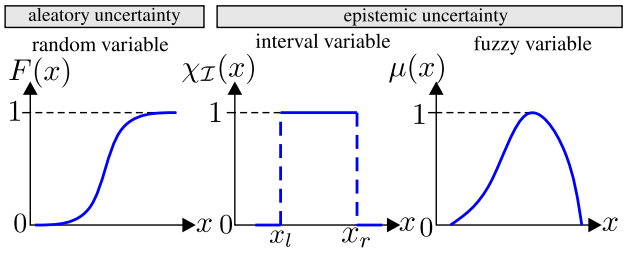

Fig. 1 Basic uncertainty models: random, interval and fuzzy variable

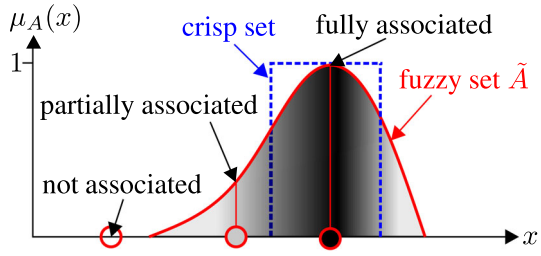

Fig. 2 Representation of a crisp and fuzzy set

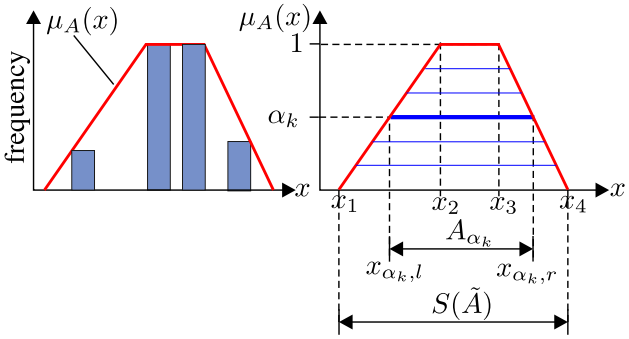

Fig. 3 Definition of a membership function based on a histogram (left) and representation of a fuzzy trapezoidal number with α-levels (right)

2 Uncertainty quantification methods for shell buckling

A reasonable modeling of shell buckling problems requires an appropriate uncertainty quantification (UQ), where various uncertainty models are selected based on available data. The objective is to address both types of uncertainties, aleatory (natural viability) and epistemic uncertainty (limited knowledge). The uncertainty models employed in this paper within the framework of VAT (fiber-steered) composite shells are briefly introduced in the following subsections. The corresponding theoretical basis is derived from [16, 56, 71].

2.1 Basis uncertainty models

The three basic uncertainty models: random, interval and fuzzy variable are depicted in Fig. 1. The natural variability (aleatory uncertainty) is determined by random variables, while the lack of knowledge (epistemic uncertainty) is quantified using interval and/or fuzzy variables. A random variable X^r is defined by the mapping operator

$$X^r : \Omega \to \mathbb{R}, \ \omega \mapsto X^r(\omega) \tag{1}$$

based on the probability space (Ω, Σ, P). Thus, each event ω of the sample space Ω is assigned a real number $X^r(\omega)$. An occurrence of $x \in \Sigma$ in the Σ-algebra is defined by the probability measure

$$P : \Sigma \to [0, 1], \tag{2}$$

which is indicated by the distribution function $F(x)$ and density function $f(x)$. These associated functions of a random variable are specified by the distribution parameters λ_X as given in [65]

$$F(x) = F(x, \lambda_X) \quad \text{and} \quad f(x) = f(x, \lambda_X). \tag{3}$$

Random variables are simulated using random number generators, for which distribution parameters λ_X–such as the mean value $E[X]$, standard deviation $\sigma[X]$, and distribution function–must be defined a priori.

This requires a large amount of data (experiments). The safety of a shell design is determined entirely by the choice of possible distribution functions and associated distribution parameters. If not enough data is available, false assumptions can be generated in a probabilistic approach. This inherent uncertainty due to a small data set is referred to as epistemic uncertainty, which can be modeled with intervals and fuzzy variables. The definition of a fuzzy variable $\tilde{A}$ as a possibility measure

$$\begin{aligned} &\tilde{A} = \{(x, \mu_A(x)) \mid x \in \mathbb{R}\}, \\ &\mu_A(x) : \mathbb{R} \to [0, 1], \\ &\sup_{x \in \mathbb{R}} [\mu_A(x)] = 1 \end{aligned} \tag{4}$$

contains a membership function $\mu_A(x)$, that allows to gradually evaluate the membership of an element x to a set. In Fig. 2, a crisp set and a fuzzy set are depicted.

An element can assume intermediate states between "fully associated" with $\mu_A(x) = 1$ or "not associated" with $\mu_A(x) = 0$. All elements in the crisp set belong to the set with the same membership $\mu(x) = 1$. The crisp set represents a specific case of a fuzzy variable: the interval. The definition of a membership function can be performed based on linguistic assessments and expert knowledge. For this purpose, existing data prepared in a histogram can serve, see Fig. 3 (left).

In contrast to define distribution parameters λ_X of a random variable, even a small amount of data may be sufficient to define a membership function. This allows an evaluation based on available (few) data of the input parameters, e.g., fiber orientation angle of a VAT composite shell. In this context, experts can estimate the extreme values of the fiber angles based on the manufacturing process. Thus, the epistemic uncertainty (incomplete data) can be quantified by including expert knowledge. In this contribution, only convex trapezoidal fuzzy numbers are defined using the following notation

$$\tilde{A} = \langle x_1, x_2, x_3, x_4 \rangle \tag{5}$$

as depicted in Fig. 3 (right). The restriction to be convex means a monotonic decrease on both sides of the peak level at $\mu(x) = 1$. However, different shapes of the membership function are possible, e.g., triangles or non-linear branches.

The numerical analysis with fuzzy variables requires the discretization of the membership function into α-levels

$$A_{\alpha_k} = \{x \in \mathbb{R} \mid \mu_A(x) \geq \alpha_k\}. \tag{6}$$

These α-level sets with $\alpha \in (0; 1]$ are crisp subsets $[x_{\alpha_{k,l}}, x_{\alpha_{k,r}}]$ (intervals) of the support $S(\tilde{A})$. This is the basis for the uncertain buckling analysis presented in Sect. 2.4, where the interval bounds of the fuzzy output variable on each α-level have to be calculated.

A combination of the presented basic uncertainty models leads to advanced uncertainty models. For example, a definition of at least one distribution parameter λ_X in Eq. (3) as a fuzzy variable results into a fuzzy-valued probability distribution function. This advanced uncertainty model is called fuzzy probability based random variable (fp-r). Another possible uncertainty model to combine fuzzy and random quantities is the model fuzzy randomness (fr), where the combination is achieved by stochastic parametrization. A term to describe the mixture of different uncertainty models is the concept of "polymorphic" uncertainty modeling. This concept is introduced by Graf et al. [31, 32]. The main idea of this approach is the consideration of more than one uncertainty characteristic in one parameter [32]. Preliminary contributions are, e.g., Möller et al. [58], Beer [3], Reuter [62] and Pannier et al. [60].

The focus of the present paper is to investigate the influence of aleatory and epistemic uncertainties on the buckling behavior of VAT composites and how to consider the uncertainties in an optimization process. For this purpose, aleatory and epistemic uncertainties are not mixed.

2.2 Fuzzy functions—Spatial modeling of epistemic uncertainty

When input parameters vary in time or space, their epistemic uncertainties also vary temporally and spatially. Interval fields [15, 70] and fuzzy fields [35, 36] are suitable models for spatial modeling of epistemic uncertainty. In this contribution, fuzzy functions are used. The term "fuzzy fields" is intentionally avoided to prevent misunderstanding by analogy with "random fields", which are described in the next Sect. 2.3. Random fields are characterized by their correlation structure, which allows to model the spatial dependency of uncertainty. An idea for such an equivalent spatial dependency concept for fuzzy fields is proposed in [35, 36]. It is important to note that the following definition of "fuzzy function" does not consider such an interaction concept.

A fuzzy function $\tilde{z}(t)$ is defined by the uncertain mapping of crisp variables $t \in \mathbb{T}$

$$\tilde{z}(t) \colon \mathbb{T} \overset{\sim}{\rightarrow} \mathcal{F}(\mathbb{Z}). \tag{7}$$

The set of all fuzzy sets of the fundamental set $\mathbb{Z} \subseteq \mathbb{R}$ is denoted by $\mathcal{F}(\mathbb{Z})$. From Eq. (7) follows

$$\tilde{z}(t) = \{\tilde{z}(t_k) \mid t \in \mathbb{T},\ k = 1, 2.3, \dots\}, \tag{8}$$

where the fuzzy function $\tilde{z}(t)$ assigns one fuzzy variable $\tilde{z} \in \mathcal{F}(\mathbb{Z})$ to each crisp $t_k \in \mathbb{T}$.

If the fundamental set $\mathbb{T}$ signifies the time axis, the fuzzy function $\tilde{z}(t)$ is identified as a fuzzy process. In this contribution, a fuzzy function $\tilde{z}(\boldsymbol{x})$ is used to describe the epistemic uncertainty of the fiber path, that is a function based on two-dimensional spatial coordinates $\boldsymbol{x} = (x, y) \in \Omega \subseteq \mathbb{R}^2$ on the surface of the shell structure.

For the numerical implementation, the so-called bunch parameter representation has proven to be beneficial [56, 57]. Consequently, the fuzzy function can be expressed in parametric form as a function depending on the fuzzy bunch parameter $\tilde{\boldsymbol{s}}$ and crisp arguments $\boldsymbol{x}$

$$\tilde{z}(\boldsymbol{x}) = z(\tilde{\boldsymbol{s}}, \boldsymbol{x}) \quad \text{with} \quad \tilde{\boldsymbol{s}} = \{\tilde{s}_1, \tilde{s}_2, \dots\}. \tag{9}$$

The fuzzy bunch parameter $\tilde{\boldsymbol{s}}$ contains all pre-defined fuzzy input parameters, e.g., fuzzy fiber orientation angles for steering the fiber path. In general, Eq. (8) leads to

$$z(\tilde{\boldsymbol{s}}, \boldsymbol{x}) = \{z(\tilde{\boldsymbol{s}}, \boldsymbol{x}_i) \mid \boldsymbol{x} \in \Omega,\ i = 1, 2, 3, \dots\}. \tag{10}$$

From another perspective, Eq. (10) means that for a vector of crisp input parameters $\boldsymbol{s} = \{s_1, s_2, \dots\}$ and the corresponding membership values $\mu(s_1), \mu(s_2), \dots$, a crisp function $z(\boldsymbol{x}) = z(\boldsymbol{s}, \boldsymbol{x})$ is obtained with $\mu(z(\boldsymbol{x})) = \mu(\boldsymbol{x})$ [56]. In

terms of the presented application of fiber steering, it follows that a crisp fiber path can be obtained. The numerical processing of fuzzy functions requires in addition to the α-level discretization, as depicted in Fig. 3 (right), a point discretization of the arguments $\boldsymbol{x}$. This discrete fuzzy function is defined by its values at the points in space $\boldsymbol{x}_i \in \Omega$ in Eq. (10). If the fuzzy function is defined, e.g., on a finite element (FE) model, the number of discretization points, numnp, corresponds to the number of FE nodes. Then, the fuzzy function can be expressed as:

$$\tilde{z}(\boldsymbol{x}) = \{z(\tilde{\boldsymbol{s}}, \boldsymbol{x}_1), z(\tilde{\boldsymbol{s}}, \boldsymbol{x}_2), \ldots, z(\tilde{\boldsymbol{s}}, \boldsymbol{x}_{\text{numnp}})\}, \tag{11}$$

where a sequence of fuzzy variables is represented on the FE model.

2.3 Random fields—Spatial modeling of aleatory uncertainty

The imperfection sensitivity of VAT composite shell is analyzed, where the spatial aleatory uncertainty of geometrical shell imperfections are modeled with random fields. Therefore, a brief summary is provided on the fundamentals of random field modeling based on [68, 71, 74].

A random field $w^{\text{rf}}(\boldsymbol{x}, \theta)$ is in a mathematical sense a collection of random variables defined as follows:

$$\{w^{\text{rf}}(\boldsymbol{x}, \theta) \mid \boldsymbol{x} \in \Omega, \theta \in \Theta\}, \quad \boldsymbol{x} = \begin{pmatrix} x \\ y \end{pmatrix}, \tag{12}$$

where the possible outcomes within the event set Θ are labeled as θ. For a fixed location $\boldsymbol{x}_0 \in \Omega$ a random variable $w^{\text{rf}}(\boldsymbol{x}_0, \theta)$ is assigned. In terms of geometric shell imperfections, a two-dimensional random field describes the geometric deviations of the shell surface coordinates. If the random field is a Gaussian random field, each point is associated with a Gaussian normal distribution, characterized by mean $\mu(\boldsymbol{x})$ and variance $\sigma^2(\boldsymbol{x})$

$$w^{\text{rf}}(\boldsymbol{x}_0, \theta) \sim \mathcal{N}(\mu(\boldsymbol{x}_0), \sigma^2(\boldsymbol{x}_0)). \tag{13}$$

Moreover, a specific realization of a random field corresponding to a given event θ_0 can be indicated as:

$$w_0^{\text{rf}}(\boldsymbol{x}) := w^{\text{rf}}(\boldsymbol{x}, \theta_0). \tag{14}$$

The covariances of two points $\boldsymbol{x}_i(x_i, y_i)$ and $\boldsymbol{x}_j(x_j, y_j)$ are given by the autocovariance function

$$\begin{aligned} &C(\boldsymbol{x}_i, \boldsymbol{x}_j) \\ &= E[(w^{\text{rf}}(\boldsymbol{x}_i) - \mu(\boldsymbol{x}_i))(w^{\text{rf}}(\boldsymbol{x}_j) - \mu(\boldsymbol{x}_j))], \end{aligned} \tag{15}$$

which leads to the autocorrelation function (acf)

$$\rho(\boldsymbol{x}_i, \boldsymbol{x}_j) = \frac{C(\boldsymbol{x}_i, \boldsymbol{x}_j)}{\sigma(\boldsymbol{x}_i)\sigma(\boldsymbol{x}_j)} \tag{16}$$

by normalization with the standard deviations $\sigma(\boldsymbol{x}_i)$ and $\sigma(\boldsymbol{x}_j)$. A homogeneous covariance function is defined as follows:

$$C(d) = \sigma^2 \rho(d), \tag{17}$$

where the acf is a function of the Euclidian distance d between two points $\boldsymbol{x}_i, \boldsymbol{x}_j$ (e.g., FE nodes)

$$\begin{aligned} &\rho(\boldsymbol{x}_i, \boldsymbol{x}_j) = \rho(d) \quad \text{with} \\ &d = |\boldsymbol{x}_j - \boldsymbol{x}_i| = \sqrt{(x_j - x_i)^2 + (y_j - y_i)^2}. \end{aligned} \tag{18}$$

For the investigations in this paper, the following quadratic exponential acf is chosen to generate the homogeneous covariance function in Eq. (17)

$$\rho(d) = \exp\left[-\frac{d^2}{\ell_c^2}\right]. \tag{19}$$

In this Eq. (19), ℓ_c is the correlation length, which controls how quickly the acf falls off for larger distances d. If the correlation length ℓ_c tends to infinity or the distance between two separated points is zero, the exponential covariance function converges to the value one. This means that two points are fully dependent (correlated). In contrast, small correlation lengths lead to uncorrelated fields (wavy shell imperfections). The random field is termed weakly homogeneous when, in addition, the first two moments (mean and variance) within the domain Ω remain constant (translationally invariant)

$$\mu(\boldsymbol{x}) = \mu \quad \text{and} \quad \sigma^2(\boldsymbol{x}) = \sigma^2. \tag{20}$$

A numerical treatment to generate random fields requires a discretization technique. For this purpose, the Karhunen-Loève Expansion (KLE) is used. This series expansion of the weakly homogeneous random field in a discrete form is defined as follows:

$$w^{\text{rf}}(\boldsymbol{x}, \theta) = \mu + \sigma \sum_{i=1}^{M} \sqrt{\lambda_i}\, \xi_i(\theta)\, \varphi_i(\boldsymbol{x}), \tag{21}$$

which defines the random geometric deviations of the shell. Therein, $\xi_i(\theta)$ is a standard normal distributed random variable, $\varphi_i(\boldsymbol{x})$ the eigenfunction and λ_i the eigenvalue of the covariance matrix formulated on the FE mesh with M nodes. This covariance matrix can be set up using the covariance function and the specified acf in Eq. (17) and Eq. (19). The

mean value μ is set to zero to model a spatially correlated field of shell imperfections. Finally, it should be noted that for large FE models a significant number of eigenvalues and eigenfunction have to be computed and stored, which is computationally intensive. Therefore, a truncation of the KLE series is recommended for large-scale problems. For example, Lauterbach et al. [46] consider a subset of eigenvalues $N < M$, such that their sum accounts for 99 % of the total eigenvalue sum. However, no truncation of the series is required for the presented examples in this paper, as the the size of the eigenvalue problem with a maximum size of 961 eigenvalues and eigenfunctions, is computationally feasible.

2.4 Fuzzy and stochastic buckling analysis

In this paper, the following mapping is performed within the framework of fuzzy analysis

$$\varphi(\tilde{\boldsymbol{s}}, \boldsymbol{x}) \mapsto P_{\mathrm{cr}}(\tilde{\boldsymbol{s}}) = \tilde{P}_{\mathrm{cr}} \qquad \text{with} \quad \tilde{\boldsymbol{s}} = \begin{pmatrix} \tilde{\varphi}_0 \\ \tilde{\varphi}_1 \end{pmatrix}. \tag{22}$$

Thus, the fuzzy fiber path $\varphi(\tilde{\boldsymbol{s}}, \boldsymbol{x})$ is defined with the fuzzy bunch parameter $\tilde{\boldsymbol{s}}$, which contains the fuzzy fiber orientation angles $\tilde{\varphi}_0$, $\tilde{\varphi}_1$ to steer the fiber course as the input parameters. The calculation of the fuzzy buckling load P_{cr} as the output variable is performed using the so-called α-level optimization (ALO) [58]. The ALO for a two-dimensional input and one-dimensional output space is depicted in Fig. 4. Dependencies of the input variables are excluded, allowing the input space to be formed with the Cartesian product $\tilde{K}$.

The computational model $\mathcal{M}(\boldsymbol{s}) = P_{\mathrm{cr}}(\boldsymbol{s})$ represents the FE model to perform the buckling analyses. Based on the α-level discretization according to Eq. (6) and Fig. 3, the interval bounds of the fuzzy output variable $\tilde{P}_{\mathrm{cr}}$ are calculated on each α-level. To consider a specific α-level α_k, the fuzzy bunch parameters are limited by the α-level boundaries

$$\boldsymbol{s} \in [\boldsymbol{s}_{\alpha_k,l}, \boldsymbol{s}_{\alpha_k,r}] = \{\boldsymbol{s}_{\alpha_k}\}. \tag{23}$$

Solving the extreme value problems on each α-level

$$\begin{aligned} P_{\mathrm{cr},\alpha_k,l} &= \min_{\boldsymbol{s}\in\{\boldsymbol{s}_{\alpha_k}\}} [\mathcal{M}(\boldsymbol{s})] \\ P_{\mathrm{cr},\alpha_k,r} &= \max_{\boldsymbol{s}\in\{\boldsymbol{s}_{\alpha_k}\}} [\mathcal{M}(\boldsymbol{s})] \end{aligned} \tag{24}$$

lead to the corresponding α-level boundaries of the fuzzy output variable $\tilde{P}_{\mathrm{cr}}$. The search of the extreme values $\mathcal{M}(\boldsymbol{s})$ in the variable space $\{\boldsymbol{s}_{\alpha_k}\}$ can be performed with an efficient optimization algorithm. In this work, the particle swarm optimization [40] is utilized to determine the extreme values in Eq. (24). However, solving these optimization problems can be highly time-consuming for a complex computational model $\mathcal{M}(\boldsymbol{s})$. To reduce the computational effort of the ALO, it is advisable to substitute the computational model (numerical buckling analysis) with a surrogate model

$$\widehat{\mathcal{M}}(\boldsymbol{s}) \approx P_{\mathrm{cr}}(\boldsymbol{s}), \quad \boldsymbol{s} \in S(\tilde{\boldsymbol{s}}). \tag{25}$$

Thus, the optimization problem in Eq. (24) is performed on the previously generated surrogate model $\widehat{\mathcal{M}}(\boldsymbol{s})$, which is trained on the support of the fuzzy bunch parameters $S(\tilde{\boldsymbol{s}})$. For this purpose, an artificial neural network (ANN) is used as a surrogate model.

Furthermore, the stochastic buckling analysis considering spatially varying aleatory uncertainty is performed with a sampling-based approach in form of a Monte-Carlo-Simulation (MCS) to solve the following mapping

$$(\varphi(\boldsymbol{x}), w^{\mathrm{rf}}(\boldsymbol{x}, \theta)) \mapsto P_{\mathrm{cr}}(\theta). \tag{26}$$

Geometric imperfections are generated as random fields (input) to calculate the stochastic buckling load $P_{\mathrm{cr}}(\theta)$ (output) for a deterministic fiber path $\varphi(\boldsymbol{x})$. Subsequently, second-order statistics, including the mean $E[P_{\mathrm{cr}}]$, standard deviation $\sigma[P_{\mathrm{cr}}]$, and coefficient of variation $CV[P_{\mathrm{cr}}] = \sigma[P_{\mathrm{cr}}]/E[P_{\mathrm{cr}}]$, are analyzed.

3 Optimization under uncertainties

The optimization objectives for shell designs under buckling conditions often involve conflicting objectives, such as maximizing buckling resistance while minimizing mass. This requires a multi-objective optimization strategy. As shown in the previous section, an uncertainty analysis leads to uncertain structural (buckling) responses. The existing aleatory and epistemic uncertainties cannot be neglected in decision-making assisted by numerical design optimization [67]. A subsequent optimization needs a post-processing of the uncertain output quantities to obtain information about the robustness and performance with respect to the design parameters [10]. In the following, the theoretical basics of multi-objective design optimization based on [10, 67] are introduced for VAT composite shells.

3.1 Fitness evaluation

A classical optimization problem definition is

$$\begin{aligned} &\min_{\boldsymbol{x}_d\in\mathcal{D}} f(\boldsymbol{x}_d, \boldsymbol{x}_a) \\ &\text{subject to:} \\ &\qquad h_i = 0 \quad \text{for} \quad i = 1, 2, \ldots, n_h \\ &\qquad g_j \le 0 \quad \text{for} \quad j = 1, 2, \ldots, n_g. \end{aligned} \tag{27}$$

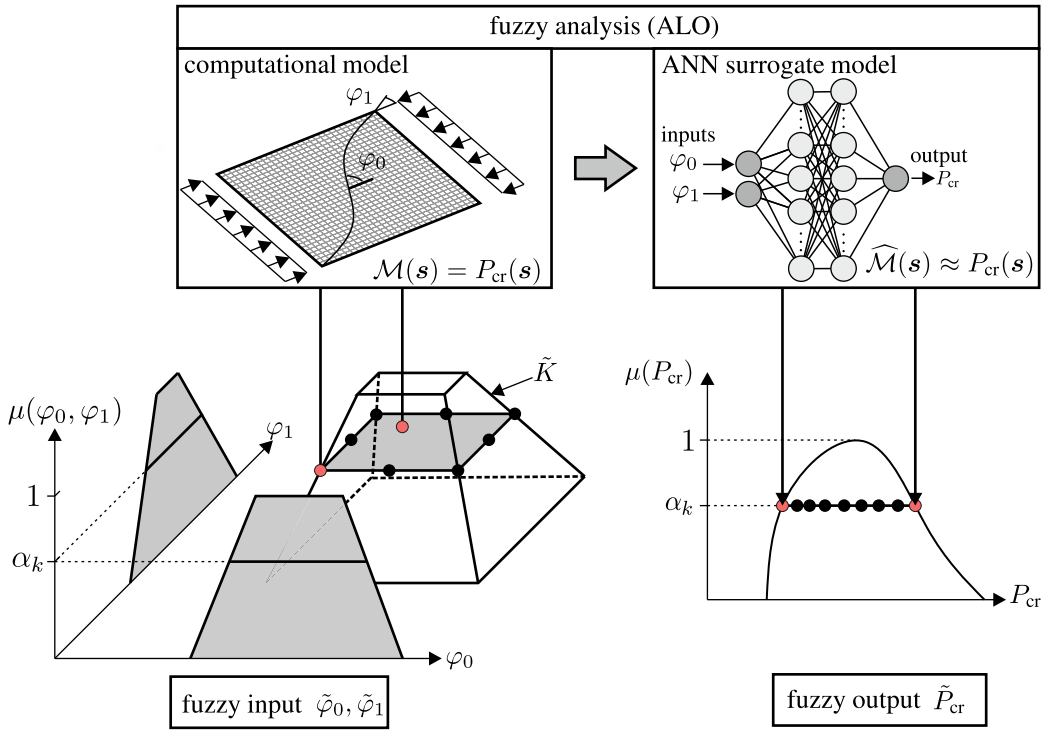

Fig. 4 Fuzzy analysis of a two-dimensional input and one-dimensional output space using the α-level optimization (ALO) and artificial neural network (ANN) as surrogate model

Therein, $f(\boldsymbol{x}_d, \boldsymbol{x}_a)$ is the objective function and $\mathcal{D}$ represents the design space with the associated vector of the design variables $\boldsymbol{x}_d$. The vector $\boldsymbol{x}_a \in \mathcal{P}$ contains the a priori parameters of the a priori space $\mathcal{P}$, which are fixed and cannot be modified during the optimization process. In addition, equality h_i and inequality constraints g_j can be considered [67].

For buckling optimization problems, the objective function $f(\boldsymbol{x}_d, \boldsymbol{x}_a)$ is often defined as the mass of the structure subject to manufacturing constraints. Possible design variables of VAT composite shells are the layer thickness, number of layers and the fiber orientation angles. For CTS/RTS manufactured VAT shells, the fiber orientation angles cannot be larger than 70°, resulting in inequality constraints $0° \leq T_i \leq 70°$ for $i = 0, 1$, see, e.g., in [49].

Alternatively, the objective function represents the buckling load, expressed as $f(\boldsymbol{x}_d, \boldsymbol{x}_a) = P_{\mathrm{cr}}(\boldsymbol{x}_d, \boldsymbol{x}_a)$, where the single objective is denoted by the buckling load P_{cr} and the design variables are the fiber orientation angles φ_0 and φ_1. The buckling optimization problem is then to maximize the buckling load, formulated as follows:

$$\max_{\boldsymbol{x}_d \in \mathcal{D}} P_{\mathrm{cr}}(\boldsymbol{x}_d, \boldsymbol{x}_a) \Leftrightarrow \min_{\boldsymbol{x}_d \in \mathcal{D}} -P_{\mathrm{cr}}(\boldsymbol{x}_d, \boldsymbol{x}_a). \tag{28}$$

This buckling optimization task without constraints is extended to consider uncertainties in the present paper. In a classical (deterministic) buckling design optimization only the structural response (performance of the structure) can be considered in the decision making process. The various types of uncertainty are not taken into account. Despite a crisp objective function, an uncertainty quantification of the design parameters $\boldsymbol{x}_d$ results in uncertain objectives, as illustrated in Fig. 5.

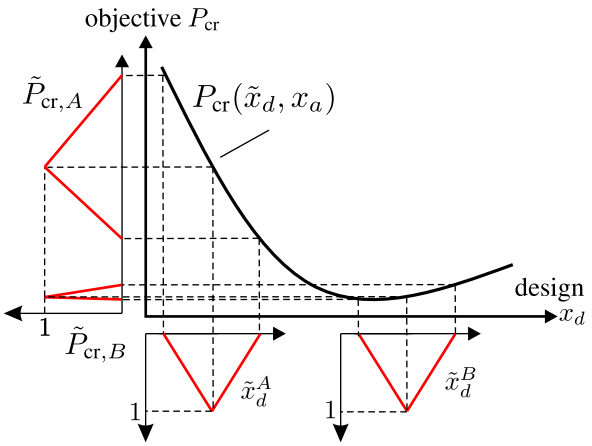

Fig. 5 Buckling optimization with uncertain design parameters and a crisp objective function

In addition to the design parameters, the a priori parameters in the vector $\boldsymbol{x}_a$ are also subject to uncertainty in this paper. The random geometric deviations from the random field model are represented by the vector $\tilde{\boldsymbol{x}}_a = \{w^{\mathrm{rf}}(\boldsymbol{x}_1, \theta), w^{\mathrm{rf}}(\boldsymbol{x}_2, \theta), \ldots, w^{\mathrm{rf}}(\boldsymbol{x}_M, \theta)\}$. These random geo-

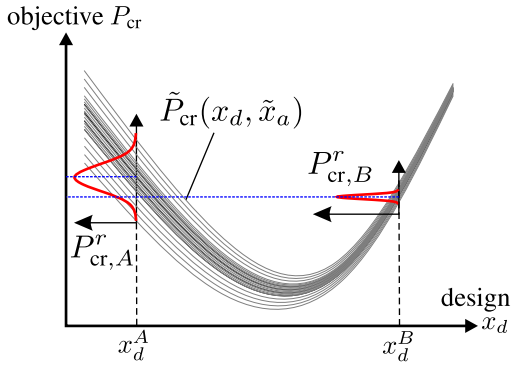

Fig. 6 Buckling optimization with crisp design parameters and an uncertain objective function

metric deviations cannot be modified during the optimization process. However, this results in an uncertain objective function as depicted in Fig. 6.

In case of uncertain design parameters $\tilde{\boldsymbol{x}}_d$ or an uncertain objective function $\tilde{P}_{\mathrm{cr}}(\boldsymbol{x})$ the formulation in Eq. (27) leads to uncertain buckling optimizations

$$\max_{\boldsymbol{x}_d \in \mathcal{D}} P_{\mathrm{cr}}(\tilde{\boldsymbol{x}}_d, \boldsymbol{x}_a) \quad \text{or} \tag{29}$$

$$\max_{\boldsymbol{x}_d \in \mathcal{D}} \tilde{P}_{\mathrm{cr}}(\boldsymbol{x}_d, \tilde{\boldsymbol{x}}_a). \tag{30}$$

In [67], a general representation of the optimization problem $\min_{\boldsymbol{x}_d \in \mathcal{D}} \tilde{f}(\tilde{\boldsymbol{x}}_d, \tilde{\boldsymbol{x}}_a)$ is introduced, where both vectors $\tilde{\boldsymbol{x}}_d$ and $\tilde{\boldsymbol{x}}_a$ are uncertain.

In Fig. 5 and Fig. 6, two design points x_d^A, x_d^B with their corresponding uncertain objectives are shown. If at least one design parameter is uncertain, e.g., one of the fiber orientation angles is defined as a fuzzy triangular variable $\tilde{\varphi}_0$ or $\tilde{\varphi}_1$ represented by $\tilde{x}_d$, then the buckling load as the objective also becomes a fuzzy variable $\tilde{P}^A_{\mathrm{cr}}$, $\tilde{P}^B_{\mathrm{cr}}$ derived from a precise objective function $P_{\mathrm{cr}}(\tilde{x}_d)$, as depicted in Fig. 5. In Fig. 6, the uncertain objective function $\tilde{P}_{\mathrm{cr}}(x_d)$ results from the random geometric imperfections. Although the design parameters are not uncertain, an uncertain objective emerges, represented in this case by random variables $P^r_{\mathrm{cr},A}$ and $P^r_{\mathrm{cr},B}$. In summary, for both cases, which are investigated in this paper, the single objective is uncertain defined by the following mappings

$$P_{\mathrm{cr}}(\tilde{\boldsymbol{x}}_d, \boldsymbol{x}_a) \mapsto \tilde{P}_{\mathrm{cr}} \tag{31}$$

$$\tilde{P}_{\mathrm{cr}}(\boldsymbol{x}_d, \tilde{\boldsymbol{x}}_a) \mapsto P^r_{\mathrm{cr}}. \tag{32}$$

To evaluate the fitness in presence of uncertainties, the uncertain output quantities have to be post-processed to obtain comparable scalar values. For this purpose, uncertainty reduction measures given in [67] are used. The term is further discussed in [10] and renamed to information reduction measurements (IRMs), which describes to reduce an uncertain output quantity to deterministic values. IRMs are subdivided into representative measures $\mathfrak{M}$ and uncertainty quantifying measures $\mathfrak{U}$. Representative measures $\mathfrak{M}$ are physical values to optimize the performance and uncertainty quantifying measures $\mathfrak{U}$ are used to evaluate the robustness of a structure.

In this context, the term "performance" can be used to describe the buckling resistance. For a high-performance VAT composite shells, generally substantial buckling loads are expected. The term "robustness" is used for various definitions in engineering. In structural design, robust structures are those that consistently maintain optimal performance under environmental fluctuations [5].

As an extension to probabilistic structural design, epistemic uncertainties are defined for all "fluctuating parameters" in addition to aleatory uncertainties. Various IRMs can be formulated to assess both the performance and robustness of a structure. In Table 1 and Fig. 7, the IRMs utilized in this paper are presented with respect to aleatory and epistemic uncertainty, following the notation introduced in [10].

When considering aleatory uncertainty, the standard deviation $\mathfrak{U}_\sigma(P^r_{\mathrm{cr}})$ and the coefficient of variation $\mathfrak{U}_{\mathrm{CV}}(P^r_{\mathrm{cr}})$ serve as a measure of robustness, whereas the mean of the random buckling loads $\mathfrak{M}_\mu(P^r_{\mathrm{cr}})$ serves as a measure of performance. If the buckling loads are represented as fuzzy variables, performance can be assessed using the centroid $\mathfrak{M}_{x_S}(\tilde{P}_{\mathrm{cr}})$, while robustness can be quantified by considering the area $\mathfrak{U}_A(\tilde{P}_{\mathrm{cr}})$ of the fuzzy output variable.

Employing various IRMs for fitness comparison may reveal conflicts between robustness and performance. Such a conflict is also visualized in Fig. 5 and Fig. 6. The mean or centroid (performance measures) of the resulting quantities for design $\square^A$ is larger than that for design $\square^B$. However, the area and coefficient of variation (robustness measures) of the result quantities for $\square^A$ are also larger (smaller robustness) than those for $\square^B$. Pareto fronts can be employed within multi-objective design optimization to make conflicts visible, see, e.g., in [8, 11, 39]. A graphical representation of a Pareto front is illustrated in Fig. 8.

Considering that a robust structure is characterized by small values of $\mathfrak{U}$, the ideal design point is achieved by minimizing $\mathfrak{U}$ and maximizing $\mathfrak{M}$. However, the ideal point does not belong to the set of feasible results. Therefore, the Pareto front is utilized in the decision-making process, describing an optimal compromise. The Pareto front includes all design points where, conversely, a decrease in robustness is associated with an increase in performance.

Finally, the optimization problems considering uncertainties given in equations (29) and (30) can be formulated using the IRMs. It follows the multi-objective design optimization tasks

Table 1 Information reduction measures (IRMs) to evaluate the performance and robustness in a structural design under uncertainty, following the notation in [10]

Uncertainty	performance measures $\mathfrak{M}$		robustness measures $\mathfrak{U}$	
aleatory	mean	$\mathfrak{M}_\mu(P_{\text{cr}}^r) = \int_{-\infty}^{+\infty} f(P_{\text{cr}})\, P_{\text{cr}}\, dP_{\text{cr}}$	CV	$\mathfrak{U}_{\text{CV}}(P_{\text{cr}}^r) = \mathfrak{U}_\sigma(P_{\text{cr}}^r)/\mathfrak{M}_\mu(P_{\text{cr}}^r)$
[0.5cm] epistemic	centroid	$\mathfrak{M}_{x_S}(\tilde{P}_{\text{cr}}) = \int_{\min(P_{\text{cr}})}^{\max(P_{\text{cr}})} P_{\text{cr}}\, \mu(P_{\text{cr}})\, dP_{\text{cr}}$	area	$\mathfrak{U}_A(\tilde{P}_{\text{cr}}) = \int_{\min(P_{\text{cr}})}^{\max(P_{\text{cr}})} \mu(P_{\text{cr}})\, dP_{\text{cr}}$

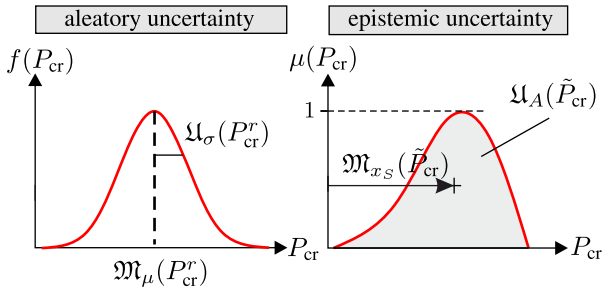

Fig. 7 Representation of performance $\mathfrak{M}$ and robustness $\mathfrak{U}$ measures for aleatory (left) and epistemic (right) uncertainties

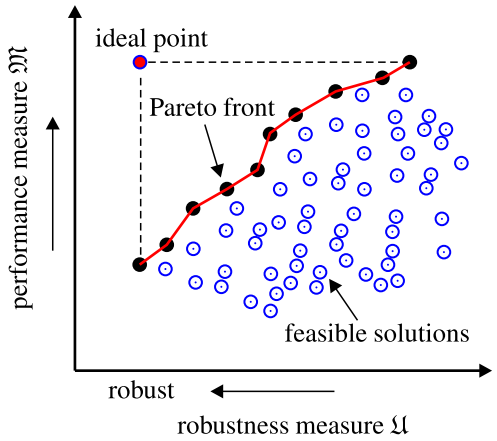

Fig. 8 Representation of a Pareto front with robustness and performance measures

$$\max_{\boldsymbol{x}_d \in \mathcal{D}} P_{\text{cr}}(\tilde{\boldsymbol{x}}_d, \boldsymbol{x}_a) = \max_{\boldsymbol{x}_d \in \mathcal{D}} \left[\mathfrak{M}(P_{\text{cr}}(\tilde{\boldsymbol{x}}_d, \boldsymbol{x}_a)); -\mathfrak{U}(P_{\text{cr}}(\tilde{\boldsymbol{x}}_d, \boldsymbol{x}_a))\right] \tag{33}$$

$$\max_{\boldsymbol{x}_d \in \mathcal{D}} \tilde{P}_{\text{cr}}(\boldsymbol{x}_d, \tilde{\boldsymbol{x}}_a) = \max_{\boldsymbol{x}_d \in \mathcal{D}} \left[\mathfrak{M}(\tilde{P}_{\text{cr}}(\boldsymbol{x}_d, \tilde{\boldsymbol{x}}_a)); -\mathfrak{U}(\tilde{P}_{\text{cr}}(\boldsymbol{x}_d, \tilde{\boldsymbol{x}}_a))\right], \tag{34}$$

where the minimization of $\mathfrak{U}$ is indicated by the negative sign. The deterministic output quantities allow for the utilization of common optimization algorithms, such as particle swarm optimization [40], to solve those minimization problems.

3.2 Multi-loop computational model and surrogate model strategy

The numerical treatment of single- or multi-objective optimization with uncertain parameters is performed based on multi-loop computational models as given, e.g., in [30, 35, 65]. The performed multi-loop computational schemes in this paper for (a) deterministic, (b) aleatory and (c) epistemic input/output parameters are depicted in Fig. 9.

The inner loop represents the deterministic computational model $\mathcal{M} = P_{\text{cr}}$, which serves as the FE model of the VAT composite shells to carry out numerical buckling analyses. In this paper, for (a) deterministic parameters and (c) epistemic uncertain parameters (fiber orientation angles as fuzzy variables), an artificial neural network (ANN) serves as a surrogate model $\widehat{\mathcal{M}} \approx P_{\text{cr}}$ to approximate the FE model.

The surrogate model can be directly used to perform the single-objective optimization for case (a). When uncertain parameters are defined as input parameters, an intermediate loop is required for uncertainty analysis, incorporating basic uncertainty models such as stochastic (b) and fuzzy analyses (c). In the stochastic analysis, the MCS is performed with random imperfections for specific fiber orientation angles to estimate the second-order statistics of the buckling load. In this contribution, no surrogate model is constructed for the stochastic design optimization according to Eq.(33). For this purpose, an advanced surrogate model strategy for random fields is required, where the buckling load have to be predicted for the random field realizations. This means, that the training space of such a surrogate model can be defined by the number of discretization points (random variables), e.g., the number of FE nodes. To construct such a surrogate model is particularly challenging for complex FE models with a large number of nodes, especially when the structure is highly sensitive to imperfections. If the fiber angles are added to the input variables, the MCS can be performed based on such a surrogate model. However, to introduce such a surrogate strategy is beyond the scope of this paper. For the stochastic design optimization in Sect. 5.2, the design space is discretized in a sufficiently fine grid. Then on each design point an MCS is run. With this approach, sufficiently accurate optimization results are achieved. However, further studies

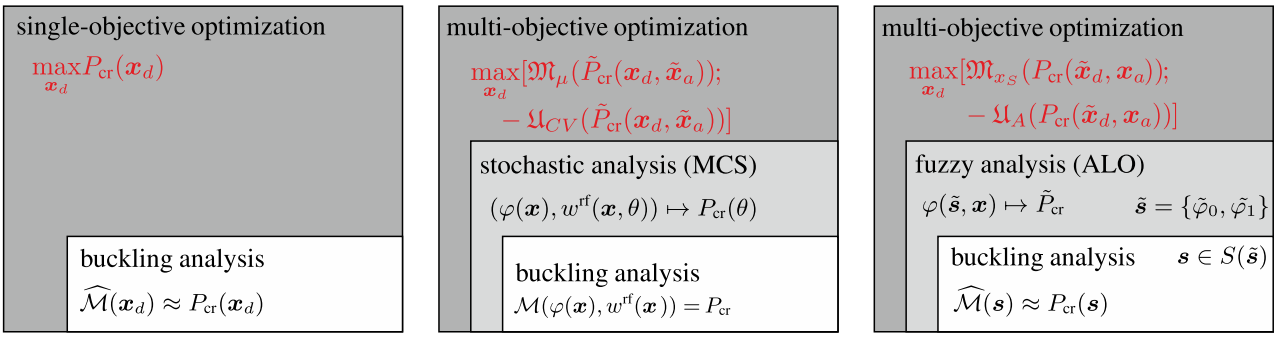

(a) deterministic (b) aleatory (c) epistemic

Fig. 9 Multi-loop computational models for different buckling design optimizations: (a) deterministic, (b) aleatory and (c) epistemic

with a larger number of design variables in the presence of uncertain imperfection fields requires an advanced surrogate model strategy. The fuzzy analysis is based on the ALO and α-level discretization using the trained ANN as presented in Fig. 4. The outer loop of Fig. 9 (c) solves the multi-objective optimization task according to Eq. (34). For this purpose, the particle swarm optimization [40] uses the ANN surrogate model to obtain fast solutions at specific design points. The IRMs listed in Table 1 are computed and potential conflicts between the objectives are visualized through Pareto fronts.

The primary focus of this paper is to demonstrate the influence of epistemic and aleatory uncertainties on optimized solutions, as well as to uncover potential conflicts between the robustness and performance of VAT composite shells. Therefore, aleatory and epistemic uncertainties are decoupled and analyzed separately in a multi-objective optimization approach. As an outlook, both uncertainty characteristics aleatory (random fields) and epistemic (fuzzy fiber path) should be considered simultaneously within the framework of polymorphic uncertainty modeling, as presented in [26]. Then, a nested uncertainty analysis (fuzzy stochastic analysis) has to be performed to solve the following mapping

$$(\tilde{\boldsymbol{s}}, w^{\mathrm{rf}}(\boldsymbol{x}, \theta)) \mapsto \tilde{P}_{\mathrm{cr}}(\theta) \quad \boldsymbol{s} \in S(\tilde{\boldsymbol{s}}). \tag{35}$$

To solve a multi-objective optimization problem for the polymorphic uncertainty modeling can lead to a high computational effort. Therefore, advanced surrogate model strategies can be used, such as the multi-level surrogate modeling approach described in [30] or a multi-fidelity strategy to estimate the second-order statistics of buckling loads by exploiting the correlations between linear and nonlinear buckling analysis results, as discussed in [19, 20]. In terms of a reliability-based optimization, a reliability problem is nested in the optimization task, where the objective is to minimize the failure probability [17]. Under polymorphic uncertainties, the failure probabilities are uncertain. This means that an additional loop for the interval or fuzzy analysis has to be performed within the nested optimization task. An approach for structural mechanics problems based on the operator norm theorem and the maximum standard deviation is presented in [13, 14, 21]. In this framework, crisp values of the uncertain input parameters are dedicated, which define the bounds of the failure probability. Consequently, an MCS only needs to be performed on these pre-defined crisp values, leading to a significant reduction of the computational effort.

4 Fiber path modeling

The stiffness and strength of a composite laminate depend on the fiber orientation angle φ. Classical symmetric angle-ply laminates are typically defined by the notation $[\pm\varphi]_s$, where the plies are structured with alternating fiber orientations, switching between $+\varphi$ and $-\varphi$. The fibers within each layer are straight and uniform. The mechanical properties (stiffness parameters) remain constant throughout the structure, leading to the terminology of "constant stiffness" laminates.

In the concept of VAT laminates, the fiber orientation angles of each layer are distributed across the structure, by means of steering the fibers in curved paths [12]. Because of their spatially varying stiffness and strength properties defined by the fiber orientation angle, VAT composites are also referred to as "variable stiffness" laminates.

The varying fiber orientation angle is denoted as $[\pm\varphi(x)]_s$, where the pair of fiber angles vary along a defined axis, e.g., the x-direction. A mathematical formulation of the steered fiber path is essential for analyzing the structural behavior. Various fiber path definitions exist in the literature, e.g., geodesic, constant angle, constant curvature path or path with linearly varying fiber angle [6]. In this work, the common definition of linear variation of the fiber orientation angle proposed by [37] is utilized. To address epistemic uncertainties, this common deterministic fiber path definition is extended

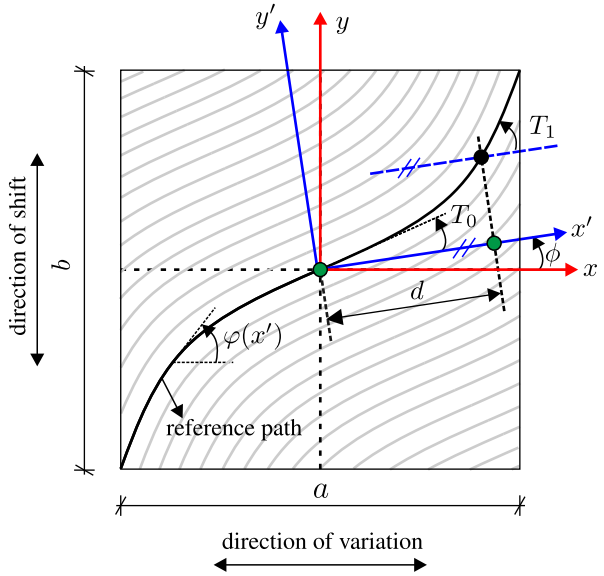

Fig. 10 Deterministic fiber path

to a fuzzy fiber path definition based on the formulations for fuzzy functions in Sect. 2.2.

4.1 Deterministic fiber path

The commonly used deterministic fiber path definition introduced by [37] is as follows:

$$\varphi(x') = \phi + (T_1 - T_0)\frac{|x'|}{d} + T_0. \tag{36}$$

In this formulation, the fiber orientation angle φ of a reference fiber path linearly varies along a direction x', from a fiber orientation angle T_0 at an arbitrary fixed starting point to the fiber orientation angle T_1 at a characteristic distance d, as depicted in Fig. 10.

To allow a rotation of the direction of fiber orientation angle variation, the x'-axis is oriented at an angle ϕ with respect to the x-axis. The reference fiber path in Eq. (36), depicted by the solid black line in Fig. 10, represents the trajectory taken by the fiber placement machine head as it lays down a band of tows [12]. To determine fiber orientation angles at different points within the x-y plane, the reference path is shifted perpendicular to the direction of variation (along the x'-axis), depicted by the light gray lines in Fig. 10. Thus, the fiber orientation angle is a function of both coordinates: $\varphi = \varphi(x, y)$.

The single curvilinear fiber path with a linear variation of the fiber orientation angle according to Eq. (10) can be calculated via the integration [72]

$$\frac{dy(x')}{dx'} = \tan\varphi(x') \Leftrightarrow y(x') = \int_{x'} \tan(\varphi(x'))\, dx', \tag{37}$$

leading to

$$y'(x') = \pm \frac{d \cdot \ln\left[\cos\left(\frac{x'\,(T_1 - T_0)}{d} + T_0 + \phi\right)\right]}{T_0 - T_1} + C. \tag{38}$$

Therein, the integration constant C defines the shift in y-direction, which can be determined by the boundary condition $y'(x' = 0) = 0$

$$C = \pm\frac{d \cdot \ln\left[\cos\left(T_0 + \phi\right)\right]}{T_0 - T_1}. \tag{39}$$

Gürdal et al. [37] introduced the notation $\phi\langle T_0|T_1\rangle$ to specify a single curvilinear layer. In this work, the orientation angle ϕ is assumed to be zero. Following this notation, laminates with stack of $\pm\langle T_0|T_1\rangle$ layer can be defined. The $\pm$ sign at the front signifies two adjacent layers with equal and opposite variations in the fiber orientation angle [37].

The fiber path according to Eq. (36) is incorporated into the shell formulation from [77], which is a four-node element with linear shape functions. This formulation employs the fiber orientation angle to convert the local material matrix of each layer into a defined global coordinate system. Initially, the fiber path defined in Eq. (36) is evaluated at the finite element (FE) nodes. Subsequently, at the element level, the transformation of the fiber orientation angle from the nodes to the four Gaussian points is performed using the isoparametric concept as follows:

$$\varphi(\xi, \eta) = \sum_{I=1}^{4} N_I(\xi, \eta)\varphi_I(x, y). \tag{40}$$

Therein, $\varphi_I(x, y)$ is a fiber orientation angle evaluated at a specific element node I using Eq. (36). This angle is interpolated to the fiber orientation angle of a desired point, such as a Gaussian point, within the isoparametric space $\varphi(\xi, \eta)$ using the linear shape functions $N_I(\xi, \eta)$.

4.2 Uncertain fiber path

The deterministic fiber path given in Eq. (36) is extended to a fuzzy function to account for epistemic uncertainty. Using the fundamental definitions in Sect. 2.2, the fuzzy fiber path can be expressed as follows:

$$\varphi(\boldsymbol{x}', \tilde{\boldsymbol{s}}) \colon \mathbb{X} \xrightarrow{\sim} \mathcal{F}(\mathbb{Z}) \;\text{ with }\; \tilde{\boldsymbol{s}} = \begin{pmatrix} \tilde{T}_0 \\ \tilde{T}_1 \end{pmatrix}, \tag{41}$$

where the fuzzy fiber orientation angles $\tilde{T}_0$, $\tilde{T}_1$ are contained as fuzzy variables in the fuzzy bunch parameter $\tilde{\boldsymbol{s}}$.

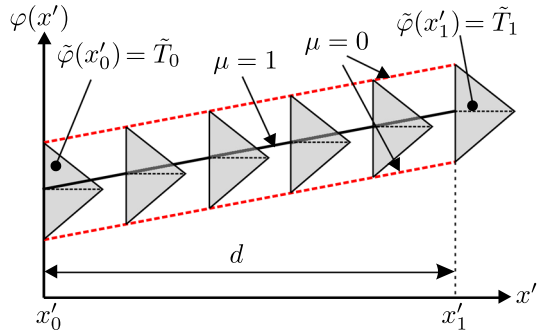

Fig. 11 Fuzzy fiber orientation angle variation as a fuzzy function

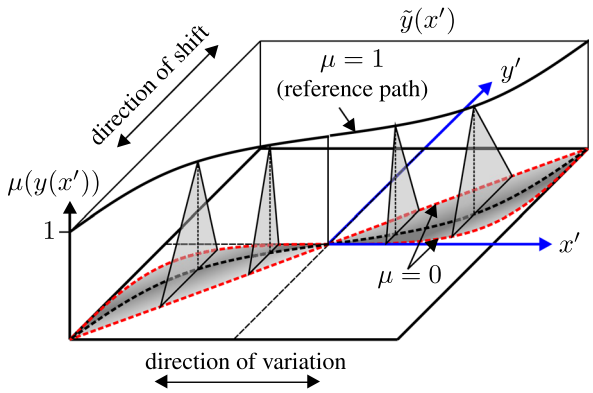

Fig. 12 Uncertain fiber path defined by a fuzzy function

Consequently, each finite element node $\boldsymbol{x}' \in \mathbb{X}$ is assigned a fuzzy fiber orientation angle $\varphi(\boldsymbol{x}', \tilde{\boldsymbol{s}}) \in \mathcal{F}(\mathbb{Z})$, which is depicted in Fig. 11. In this example, fuzzy triangular numbers are assigned for the starting angle $\tilde{\varphi}(x'_0) = \tilde{T}_0$ and the angle $\tilde{\varphi}(x'_1) = \tilde{T}_1$ at the characteristic distance d. Between these two angles, the fuzzy function varies linearly leading to the typical "Toblerone" shape. The associated angles of the outer dashed red lines have a membership of zero ($\mu = 0$). Fiber orientation angles with a membership of $\mu = 1$ are defined by the black solid line in the center. This line belongs to deterministic fiber orientation angles and within the context of a fuzzy function, it is also referred to as "trend function". The corresponding fuzzy fiber paths are depicted in Fig. 12, where the vertical axis represents the membership values. At the top of Fig. 12, the reference fiber path for $\mu = 1$ is illustrated, as shown in Fig. 10.

For fuzzy fiber orientation angles, the fiber path defined in Eq. (38) can also be expressed as a fuzzy function (field).

$$y'(\boldsymbol{x}', \tilde{\boldsymbol{s}}) \colon \mathbb{X} \xrightarrow{\sim} \mathcal{F}(\mathbb{Z}) \quad \text{with} \quad \tilde{\boldsymbol{s}} = \begin{pmatrix} \tilde{T}_0 \\ \tilde{T}_1 \end{pmatrix}. \tag{42}$$

It should be noted, that all fuzzy triangular numbers (membership functions) have the same shape in Fig. 11. When measurements show that deviations in fiber orientation angles (uncertainty) from the reference path vary significantly

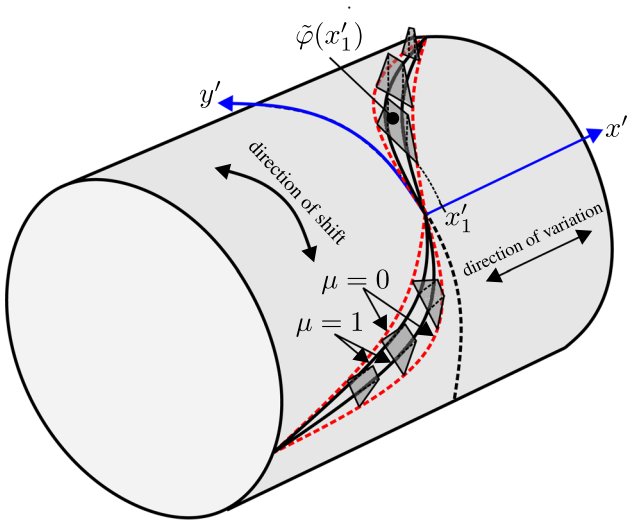

Fig. 13 Fuzzy fiber path defined on a cylindrical shell

depending on location, different membership functions can be utilized at various locations. For example, maximum angle errors can be observed near the inflection points of the tow path [42]. This expert knowledge can be included by the UQ of the fiber path.

Furthermore, the introduced definition of the fuzzy fiber path is applied to a cylindrical shell, as depicted in Fig. 13, where the fuzzy fiber orientation angles are defined using trapezoidal fuzzy numbers. The fiber path varies from the center along the axial direction and is shifted along the circumferential direction. To calculate the fiber orientation angles based on Cartesian coordinates using Eq. (36), the cylinder can be unwrapped.

5 Numerical examples

The concept of multi-objective buckling design optimization, considering both aleatory and epistemic uncertainties, is demonstrated on a VAT composite panel and cylindrical shell. The optimization results under uncertainty are compared with those obtained from classical (deterministic) design optimization approaches. The panel example is derived from [37]. To analyze the imperfection sensitivity different correlated random fields as geometric imperfection (aleatory uncertainty) are applied for two various boundary conditions. The cylindrical shell example is a test cylinder presented in [44]. Thereof, experimental data of geometrical imperfection is provided. For both examples an optimization considering epistemic uncertainties is performed, where a fuzzy fiber path is defined based on fiber orientation angle measurements from [42, 84]. The results of the multi-objective optimization are visualized by Pareto fronts to discuss a decision making of optimal fiber path configurations. This contribution

focuses on the introduction of an UQ approach with aleatory and epistemic uncertainty models in buckling design optimization. Therefore, the optimization problem is limited to fiber path parameters as the design variables. However, the proposed approach can be extended to more complex tow-steered structures with multiple layers and a larger number of degrees of freedom. This includes, for example, design variables such as shell geometry parameters, layer thicknesses and number of layers.

All uncertainty quantification methods and optimization algorithms are implemented using MATLAB [54]. The surrogate model is based on the ANN provided in MATLAB, modified to solve buckling design optimization within the multi-loop computational models shown in Fig. 9. Within this framework, the buckling analyses are the fundamental solutions, which are performed by an extended version of the general finite element analysis program (FEAP) [73]. A developed interface allows to call up FEAP in MATLAB and calculate the buckling load solutions. A geometric nonlinear quadrilateral shell element with moderate rotations from [77] is implemented in FEAP. This four-node element is based on the isoparametric concept with linear shape functions. Additionally, to avoid shear locking, the assumed natural strain (ANS) method is implemented. The element formulation is modified to integrate the fiber path model described in Sect. 4.

5.1 Basics for linear and nonlinear buckling analysis

A reliable numerical buckling analysis, serving as the inner loop of the multi-loop approach illustrated in Fig. 9, is essential for obtaining meaningful results of the uncertainty analysis and optimization task. Various strategies are available for identifying a stability point, as discussed, for instance, in [76, 78].

When linear pre-buckling is present, a linear buckling analysis can be performed to calculate stability points. For this purpose, only a single linear calculation step and solving an eigenvalue problem are necessary. The linear buckling analysis is based on the decomposition of the tangent stiffness matrix

$$\begin{aligned} \boldsymbol{K}_T &= \boldsymbol{K}_{\text{lin}} + \boldsymbol{K}_{\text{nlin}} \\ &= \boldsymbol{K}_{\text{lin}} + \boldsymbol{K}_U(\boldsymbol{u}) + \boldsymbol{K}_G(\boldsymbol{\sigma}(\boldsymbol{u})), \end{aligned} \tag{43}$$

where the stiffness matrix is partitioned into linear $\boldsymbol{K}_{\text{lin}}$ and nonlinear $\boldsymbol{K}_{\text{nlin}}$ components. Depending on the variational formulation, the nonlinear terms $\boldsymbol{K}_{\text{nlin}}$ can be identified as $\boldsymbol{K}_U$, the initial displacement matrix containing the influence of pre-buckling deformations, and $\boldsymbol{K}_G$ the geometrical matrix. Hence, the eigenvalue problem for linear buckling analysis can be formulated as follows:

$$[\boldsymbol{K}_{\text{lin}} + \Lambda \boldsymbol{K}_{\text{nlin}}]\,\boldsymbol{\varphi} = \boldsymbol{0}. \tag{44}$$

In general, the tangent stiffness matrix depends on displacement $\boldsymbol{u}$ and stress state $\boldsymbol{\sigma}(\boldsymbol{u})$ as shown in Eq. (43). However, in linear buckling analysis, the case of $\boldsymbol{u} = \boldsymbol{0}$ is studied, where the linear solution

$$\boldsymbol{K}_T(\boldsymbol{0})\boldsymbol{u}_0 = \boldsymbol{P}_0 \quad \Longleftrightarrow \quad \boldsymbol{u}_0 = \boldsymbol{K}_T^{-1}(\boldsymbol{0})\boldsymbol{P}_0 \tag{45}$$

is computed for an external load $\boldsymbol{P}_0$ with $\boldsymbol{K}_T(\boldsymbol{0}) = \boldsymbol{K}_{\text{lin}}$. The lowest eigenvalue, denoted by Λ, is utilized to increase the nonlinear components of the stiffness matrix in the eigenvalue problem given by Eq. (44). A stability point is reached for $\Lambda = 1$. The associated eigenvector $\boldsymbol{\varphi}$ is an initial post-buckling mode. When $\Lambda = 1$, the mathematical expression of the stability eigenvalue emerges

$$\begin{aligned} &(\boldsymbol{K}_{\text{lin}} + \Lambda_{\text{cr}}\boldsymbol{K}_{\text{nlin}})\boldsymbol{\varphi} = \boldsymbol{0} \\ &\quad \Leftrightarrow \boldsymbol{K}_T\boldsymbol{\varphi} = \boldsymbol{0} \\ &\quad \Leftrightarrow (\boldsymbol{K}_T - \omega\boldsymbol{1})\boldsymbol{\varphi} = \boldsymbol{0}, \end{aligned} \tag{46}$$

indicating a stability point for $\omega = 0$. In case of linear pre-buckling behavior, the critical load with the corresponding critical displacement can be computed by

$$\boldsymbol{P}_{\text{cr}} = \Lambda_{\text{cr}}\boldsymbol{P}_0, \tag{47}$$

$$\boldsymbol{u}_{\text{cr}} = \Lambda_{\text{cr}}\boldsymbol{u}_0. \tag{48}$$

In case of a nonlinear pre-buckling behavior, the results of a linear buckling analysis may significantly deviate from the correct buckling load. This requires a nonlinear buckling analysis, which involves a comprehensive geometrically nonlinear path tracking analysis, utilizing an iterative procedure such as the Newton-Raphson scheme. A reliable criterion for identifying a stability point is the change in sign of the diagonal elements of $\boldsymbol{K}_T$, which also indicates unstable equilibrium states

$$\begin{aligned} &\forall D_{ii}\ ,\ D_{ii} > 0 \rightarrow \text{stable} \\ &\exists D_{ii}\ ,\ D_{ii} = 0 \rightarrow \text{indifferent} \\ &\exists D_{ii}\ ,\ D_{ii} < 0 \rightarrow \text{unstable}. \end{aligned} \tag{49}$$

While incrementally computing the load-displacement behavior, it's possible to monitor the signs of the diagonal elements of the tangent stiffness matrix $\boldsymbol{K}_T$. If one or more diagonal elements D_{ii} turn negative, it signifies an unstable equilibrium state [76]. This criterion is utilized to determine the stability points at the end of the calculation process. Once the load state of a single sample is saved, the calculation is terminated using "task killing" within the parallelized multi-loop computational model.

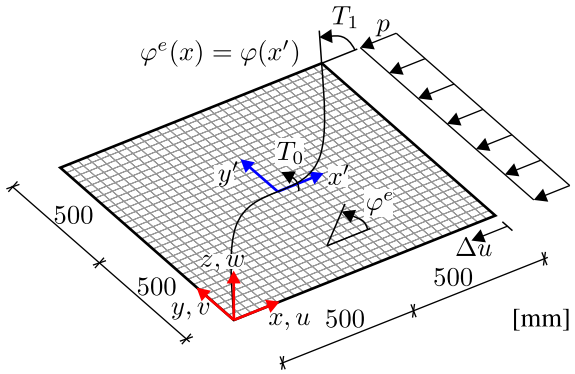

Fig. 14 FE model with load and reference fiber path of the axially loaded VAT composite panel

Table 2 Transversal isotropic material properties of the laminate

E_{11} [N/mm^2]	E_{22} [N/mm^2]	G_{12} [N/mm^2]	ν_{12} [−]
180987	10273	7170	0.28

5.2 Axially loaded VAT composite panel

At first, the presented methods are applied to an axially loaded VAT composite panel, as described in [37]. The corresponding FE model, including load and a reference fiber path, is depicted in Fig. 14. The fiber angle definition in Eq. (36) correlates with the fiber angle definition of the shell element φ^e. A FE mesh consisting of 30 × 30 elements accurately predicts the buckling behavior, allowing for representation of critical buckling modes.

The transversely isotropic material properties of the laminate, considering $G_{12} = G_{13} = G_{23}$ and $\nu_{12} = \nu_{13}$, are provided in Table 2. The panel comprises a twelve-layer laminate with a symmetric stacking sequence defined as $[\pm\langle T_0|T_1\rangle]_{3s}$. As an example, Fig. 15 illustrates a contour plot of the fiber orientation angle based on the selected FE mesh for a single layer $[+\langle 0|50\rangle]$. Each fiber-steered layer has a thickness of $t = 0.127\,\text{mm}$ leading to a total panel thickness of $h = 1.524\,\text{mm}$. The laminate is chosen to be thin enough so that strength failure is excluded.

As analyzed in [37], (a) simply supported (ssp) and (b) transverse edge restrained (ter) boundary conditions are investigated. Both cases, specifying the fixed degrees of freedom, are depicted in Fig. 16. At all edges, the rotations are free. The stress and deformation states are dependent on the boundary conditions of the transverse edges at $y = 0\,\text{mm}$ and $y = 1000\,\text{mm}$. The panels are fixed along the edge at $x = 0\,\text{mm}$ in the u-direction and subjected to a uniform end shortening Δu at the opposite edge at $x = 1000\,\text{mm}$ until the stability point is reached. For example, the load-displacement curve for the panel with the laminate $[\pm\langle 0|50\rangle]_{3s}$ and boundary conditions ter is depicted in Fig. 17.

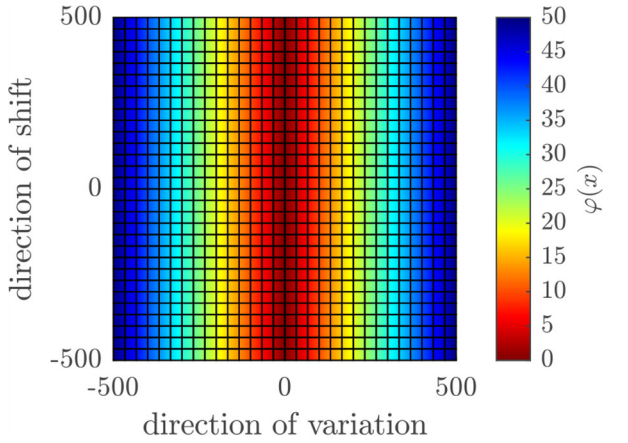

Fig. 15 Contour plot of the fiber orientation angle based on the FE mesh with the corresponding reference fiber path for a single layer $[+\langle 0|50\rangle]$

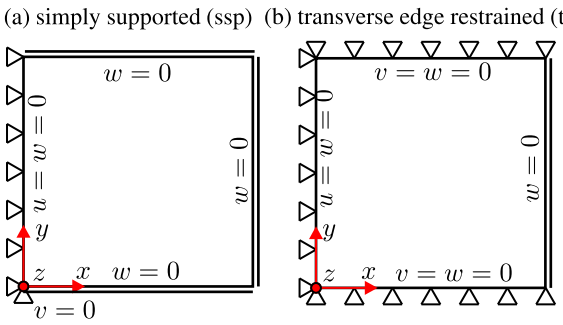

Fig. 16 Cases of boundary conditions: (a) simply supported (ssp) and (b) transverse edge restrained (ter)

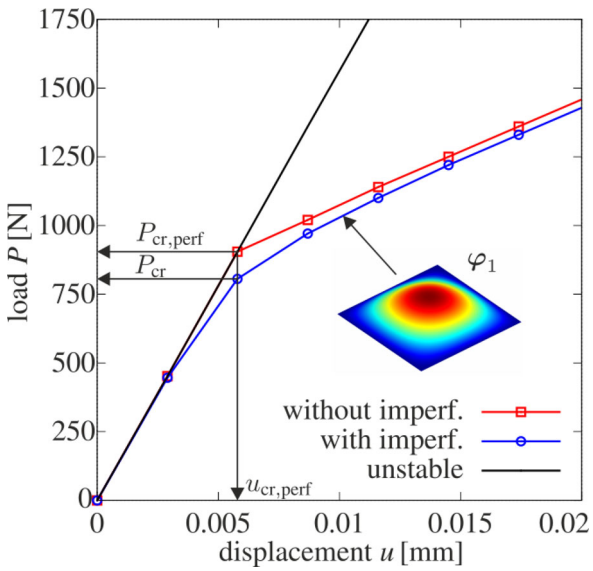

Fig. 17 VAT composite panel $[\pm\langle 0|50\rangle]_{3s}$ with boundary conditions ter: Load displacement curves stable (without geometric imperfections) and imperfect (1st eigenvector $\boldsymbol{\varphi}_1$ scaled to 0.1 mm)

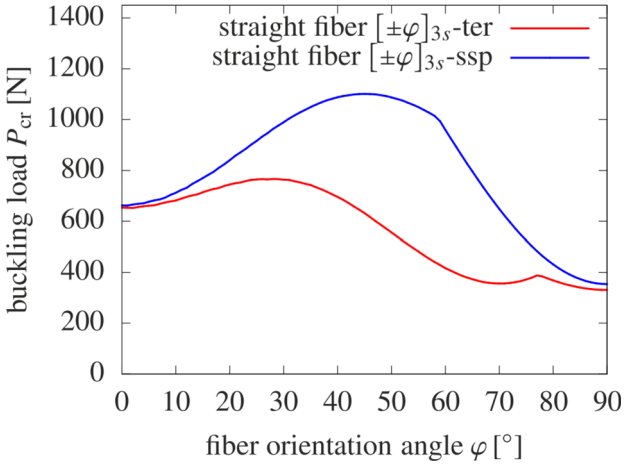

Fig. 18 Deterministic buckling optimization of SF composite panel $[\pm\varphi]_{3s}$: buckling load P_{cr} via fiber orientation angle φ

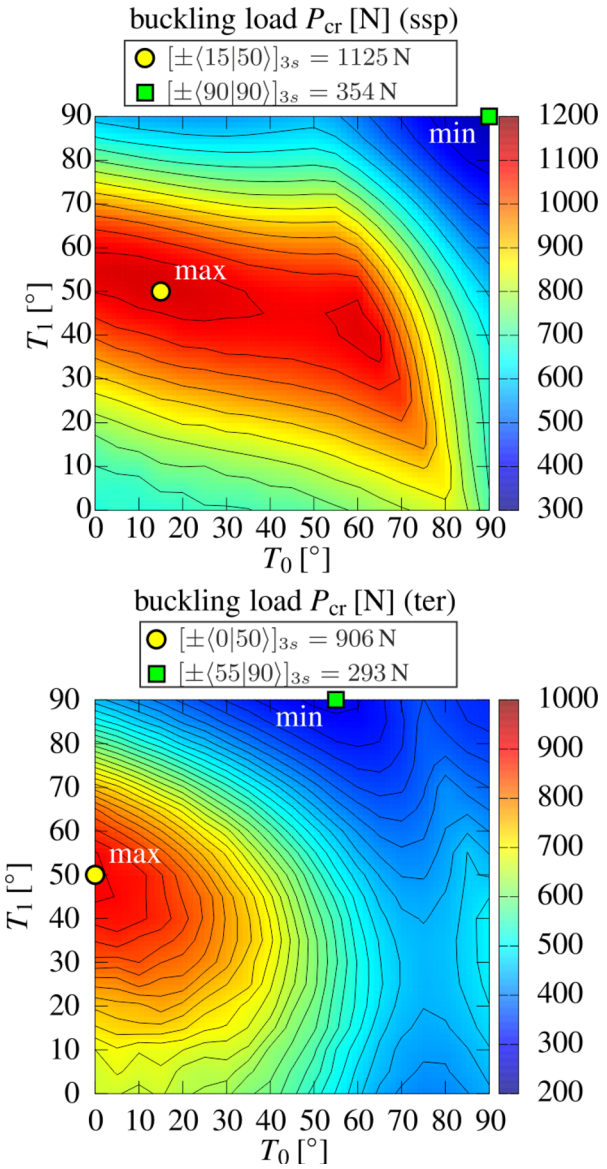

Fig. 19 Deterministic buckling optimization of the VAT composite panel: ssp (top) and ter (bottom) boundary condition

The result of the buckling load and the corresponding critical displacement of the panel without any imperfection are $P_{cr,perf} = 906\,N$ and $u_{cr,perf} = 0.0058\,mm$. Typical linear pre-buckling behavior of the flat panel can be observed. At the stability point a very small imperfection can be applied to follow the stable post-buckling path labeled as "without imperf.". If no imperfection is applied at the stability point, the post-buckling path is omitted, and the unstable path (solid black line) is followed. Additionally, the path with imperfections is depicted in Fig. 17. For this purpose, prior to loading, the first eigenvector $\boldsymbol{\varphi}_1$ is applied as nodal deviations (geometric imperfection) scaled to an amplitude of 0.1 mm. As a result, the stability point disappears. To evaluate the buckling load of the imperfect panel P_{cr}, the critical displacement $u_{cr,perf}$ corresponding to $P_{cr,pref}$ is employed as a reference point. This results in a buckling load of $P_{cr} = 806\,N$ for the imperfect panel shown in Fig. 17.

The pre-buckling behavior of the imperfect panel can be assumed to be nearly linear, especially for small imperfections. Therefore, the calculations of the geometrically imperfect panel, for example, Monte-Carlo-Simulations involving random geometric imperfections, are performed as follows in this work: the critical displacements $u_{cr,perf}$ of the panel without imperfections for all fiber path configurations are calculated using linear buckling analysis defined in Eq. (44). Subsequently, random imperfections are applied, and the panels are loaded to the critical displacement $u_{cr,perf}$, at which point the corresponding load $P_{cr}(u_{cr})$ is evaluated.

5.2.1 Deterministic optimization

First, a classical buckling optimization with deterministic design variables according to Eq. (27) is employed to illustrate how much the buckling resistance of the VAT composite panel $[\pm\langle T_0|T_1\rangle]_{3s}$ can be enhanced compared to a straight fiber (SF) $[\pm\varphi]_{3s}$ laminate. The results for both cases of boundary conditions for the SF laminate are illustrated in Fig. 18, and for the VAT laminate in Fig. 19. The design spaces are defined by the fiber orientation angles without any uncertainties. For the SF laminate, $\varphi \in [0°, 90°]$ with increments of 1° and for the VAT laminate T_0, $T_1 \in [0°, 90°]$ with a grid of 5×5. At this point, it should be noted that the optimization of the panels is idealized, and they are currently not manufacturable. For example, if manufactured using AFP, overlaps or gaps would need to be considered, while with CTS/RTS, thickness build-ups would occur. Additionally, constraints such as limiting the fiber orientation angles to no more than 70° for CTS/RTS manufacturing process are not

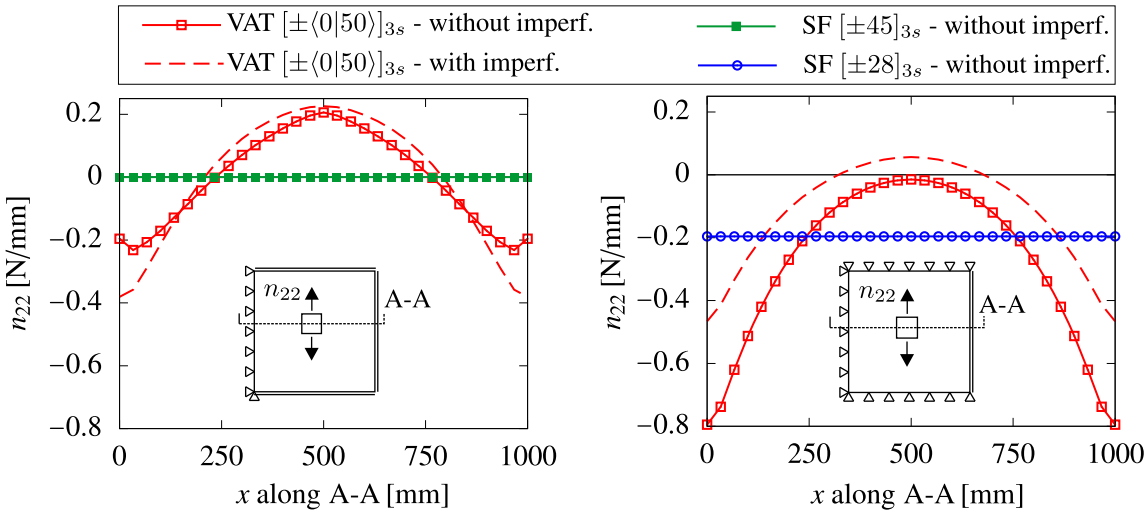

Fig. 20 Transverse normal forces n_{22} along section A-A of VAT $[\pm\langle 0|50\rangle]_{3s}$ and straight fiber (SF) $[\pm 28]_{3s}$ (ter), $[\pm 45]_{3s}$ (ssp) laminates for both boundary conditions ssp (left) and ter (right)

Table 3 Maximum buckling load max P_{cr} for the SF and VAT panel

	SF	VAT	VAT/SF
ssp	1101 N $[\pm 45]_{3s}$	1125 N $[\pm\langle 0\|50\rangle]_{3s}$	1.02
ter	766 N $[\pm 28]_{3s}$	906 N $[\pm\langle 0\|50\rangle]_{3s}$	1.18

considered. In both cases, this affects the resulting buckling loads and the overall mass of the structure.

The results of the maximum buckling load max P_{cr} and the ratios between the VAT and SF laminate are compared in Table 3. For the panel with ssp boundary conditions, only a marginal increase in the buckling load performance of approximately 2% can be observed, whereas for the ter boundary conditions, a significantly larger increase of about 18% is noted. This finding closely aligns with the results given in [37], where also an explanation of this increase is stated. For this purpose, the transverse normal forces n_{22} are calculated along a section through the center of the panel (A-A) of the VAT and SF laminates for which the maximum buckling load can be observed. The results for both boundary conditions ssp (left) and ter (right) are depicted in Fig. 20. In the case of straight fiber laminates, the transverse normal forces n_{22} are zero for ssp and constant for ter boundary conditions along section A-A. For specific fiber orientations in VAT panels, it is possible to achieve transverse normal forces n_{22} near zero at the panel center as shown in Fig. 20 (right). That is not the case with ssp boundary conditions. In the center of the investigated panel, the buckling process initiates, where the transverse normal forces n_{22} can be reduced by tailoring the fiber path. That reveals the significant optimization potential of VAT composite panels. In addition, the transverse normal forces n_{22} are depicted in Fig. 20 for the imperfect panel, where the first eigenvalue $\boldsymbol{\varphi}_1$ is applied. It is evident that the imperfection influences the stress distribution, indicating potential for reducing the imperfection sensitivity of VAT composite panels for specific fiber paths.

5.2.2 Optimization under aleatory uncertainty

In this section, a multi-objective optimization under aleatory uncertainty is presented. Aleatory uncertainty of geometric imperfections is simulated with random fields using KLE. For this purpose, the quadratic exponential acf given in Eq. (19) is chosen. The KLE series in Eq. (21) is not truncated, which means that all eigenfunctions and eigenvalues are considered. Additionally, the mean value is $\mu = 0\,\text{mm}$ and the standard deviation is $\sigma = 1\,\text{mm}$, as referenced in Eq. (21). The random fields $w^{\text{rf}}(\boldsymbol{x}, \theta)$ represent random geometric out-of-plane deviations in z-direction. Thus, different forms of imperfections can be generated for various correlation lengths and the imperfection sensitivity can be investigated. Four random field realizations $w_0^{\text{rf}}(\boldsymbol{x})$ for different correlation lengths are depicted in Fig. 21.

A small correlation length results in a highly uncorrelated and wavy geometric imperfection pattern. On the other hand, for large correlation lengths, a smooth field emerges, approaching the panel without imperfections as ℓ_c tends to infinity. These differently correlated random imperfections are applied to the panels. Following a convergence study, all Monte-Carlo-Simulations involve 500 runs. Thus, the mean and coefficient of variation (CV) of the buckling load have reached convergence.

It follows an optimization task with an uncertain objective function as illustrated in Fig. 6. The mean $\mathfrak{M}_\mu(P_{\text{cr}}^r)$ and CV $\mathfrak{U}_{\text{CV}}(P_{\text{cr}}^r)$ of the buckling load (IRMs from Table 1) are eval-

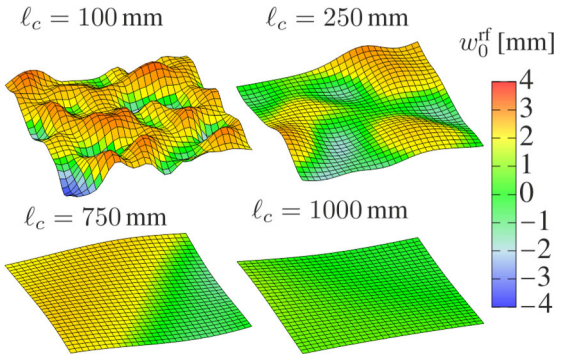

Fig. 21 Random field realizations for different correlation lengths

uated. Figure 22 presents the results for the SF panel with ssp and ter boundary conditions.

In addition to the colored curves for the different correlation lengths, the curves from Fig. 18 for the panel without imperfections are depicted by the black curve in Fig. 22 (top). For instance, smaller correlation lengths (resulting in wavy geometric imperfections) lead to lower mean values. In contrast, the mean value increases with larger correlation lengths. This can be explained that for infinitely large correlation lengths the panel without imperfections emerges. Consequently, the buckling load P_{cr} of the panel without imperfections is obtained for an infinitely large correlation length. This can be observed by the green and yellow curves for larger correlation lengths in Fig. 22 (top), which are closer to the black curve representing the panel without imperfections. Furthermore, a crossing of the mean $\mathfrak{M}_\mu(P_{\text{cr}}^r)$ and CV $\mathfrak{U}_{\text{CV}}(P_{\text{cr}}^r)$ functions can be observed in Fig. 22. For example, in Fig. 22 (top left), the function for the smallest correlation length $\ell_c = 100\,\text{mm}$ slightly crosses the function for the correlation length $\ell_c = 250\,\text{mm}$ (blue curve), and in Fig. 22 (bottom) a more distinct crossing of the CV functions is evident. As seen in Fig. 22 (bottom left), the CV functions for both smallest correlation lengths $\ell_c = 100\,\text{mm}$

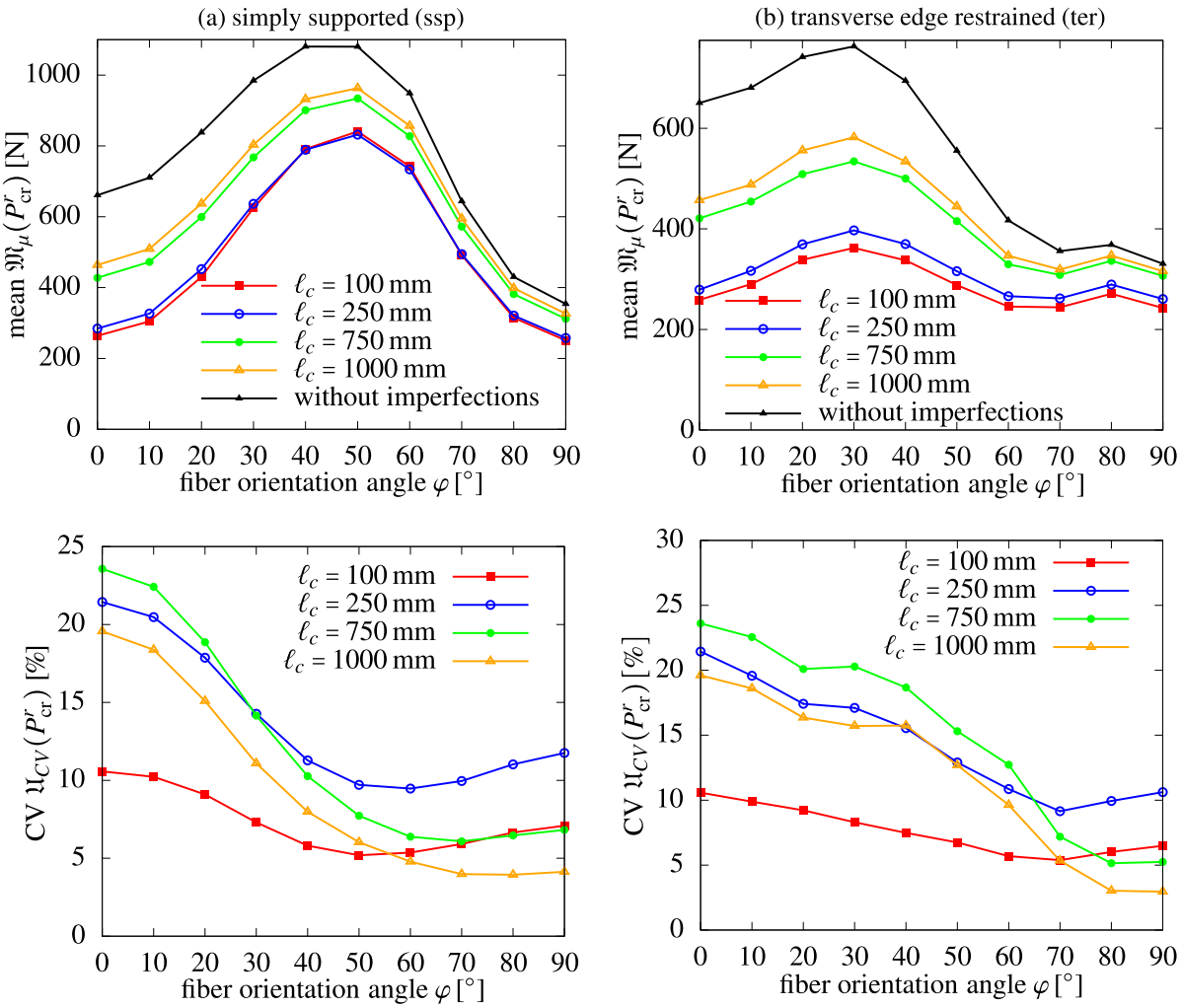

Fig. 22 SF panel $[\pm\varphi]_{3s}$ with ssp (left) and ter (right) boundary conditions under random geometric imperfections: mean (top) and CV (bottom) of the buckling load P_{cr} via fiber orientation angle φ

and $\ell_c = 250\,\text{mm}$ increase again after reaching the minimum for fiber orientation angles $\varphi > 50°$. A possible explanation for this observation is that panels with fiber orientation angles larger than 50° are more sensitive to the generated random imperfections with these specific correlation lengths. In other words, the range of possible worst-case imperfections increases, leading to an increase of the CV. This shows, that the influence of the correlation length on the stochastic buckling loads is of complex nature. Care must be taken when defining a correlation length to simulate worst-case scenarios. The smallest correlation length does not always lead to the smallest buckling load and largest variation for specific fiber orientation angles. Additional investigations and discussions on this topic are presented, for example, in [29, 46].

However, in Fig. 22 (left) for ssp boundary conditions, it can be observed that the maximum mean and the minimum CV are nearly attained for the same fiber angle configuration $[\pm 50]_{3s}$. The optimization objectives are not conflicting, which is advantageous for structural design. For ter boundary conditions in Fig. 22 (right), the maximum mean value for an SF laminate $[\pm 30]_{3s}$ is achieved. However, for this design point, the CVs are relatively high across all correlation lengths. Here is a conflict in optimizing between robustness and performance measures depending on the boundary conditions. The question arises whether this can also be observed for VAT composite panels.

A correlation length of $\ell_c = 750\,\text{mm}$ is selected to generate random imperfections for the VAT composite panel. The results for the other investigated correlation lengths do not provide any additional insights. For the multi-objective optimization, the two-dimensional design space ($T_0 \times T_1$) is discretized into a grid of 10×10 design points (100 feasible solutions). A MCS is conducted with 500 realizations for each design point. The results are illustrated in Fig. 23 for ssp and in Fig. 24 for ter boundary conditions.

In these figures, contour plots of the mean and CV, Pareto fronts with corresponding design points, and histograms of the extreme values are provided. In Fig. 23, the Pareto front of the panel with ssp boundary conditions is vertically oriented. This is a preferred behavior, indicating that the mean value of the buckling load can be increased without a significant increase in the CV. Robustness and performance measures are not in conflict. On the other hand, the Pareto front for the panel with ter boundary conditions is horizontally oriented. This indicates a significant conflict between the optimization objectives, because the performance (mean) can only be increased with a simultaneous reduction in robustness (increase of CV). In a design process, it should be considered that boundary conditions can have a significant influence on the optimization results considering uncertainties, especially if the objectives are contradictory. This becomes evident when comparing the laminate configurations for $\max P_{\text{cr}}$ (deterministic optimization), $\max \mathfrak{M}_\mu$ (maximum performance optimization), and $\min \mathfrak{U}_{\text{CV}}$ (maximum robustness optimization), as presented in Table 4. The laminate configurations vary significantly.

Table 4 Optimal design points considering aleatory uncertainties

	$\max P_{\text{cr}}$	$\max \mathfrak{M}_\mu$	$\min \mathfrak{U}_{\text{CV}}$
ssp	$[\pm\langle 15\vert 50\rangle]_{3s}$	$[\pm\langle 60\vert 40\rangle]_{3s}$	$[\pm\langle 80\vert 60\rangle]_{3s}$
ter	$[\pm\langle 0\vert 50\rangle]_{3s}$	$[\pm\langle 0\vert 50\rangle]_{3s}$	$[\pm\langle 90\vert 80\rangle]_{3s}$

5.2.3 Optimization under epistemic uncertainty

In this context, epistemic uncertainty refers to uncertainties arising from incomplete knowledge or information about fiber path modeling. Only with a high level of confidence in the alignment of actual fiber orientation angles to their desired values can laminate designers integrate the fiber orientation angle as a design variable across the entire structure, resulting in highly optimized VAT composite structures [84]. If this is not possible, the uncertainties of the fiber path have to be quantified. Due to a lack of available data, it is not advisable to define distribution functions with their parameters, such as for the fiber orientation angle. Therefore, the epistemic uncertainty of the fiber path is represented by fuzzy functions. The theoretical foundations are discussed in Sect. 4.2.

The uncertainty quantification is based on the measurements presented in [42], where manufacturing characteristics such as material properties, layup accuracy, and thickness variation of the CTS technique are experimentally examined. In [42], it is stated that the maximum angle error near the inflection points is approximately 5° and usually in the range of ±2°. Based on this statement, no random variable can be defined for the fiber orientation angle. However, this expert knowledge can be quantified with a fuzzy variable. This emphasizes another advantage of the approach presented in this work: the incorporation of expert knowledge expressed through statements regarding the uncertainties in modeling VAT composites. Based on the statements two fuzzy trapezoidal numbers for the variation of the fiber orientation angles ΔT_0 and ΔT_1 are defined as follows:

$$\begin{aligned} \Delta\tilde{T}_0 &= \langle -5, -2, +2, +5\rangle \\ \Delta\tilde{T}_1 &= \langle -5, -2, +2, +5\rangle. \end{aligned} \tag{50}$$

The one-dimensional fuzzy number, assumed to be equal for both angle variations ΔT_0 and ΔT_1, is depicted in Fig. 25. The assertion that the fiber orientation angle typically falls within the range of ±2° leads to defining a membership of one within this interval. Beyond these limits, the membership decreases linearly to zero for $\Delta T_0 = \Delta T_1 = \pm 5°$. The maximum angle variation of approximately 5° can only

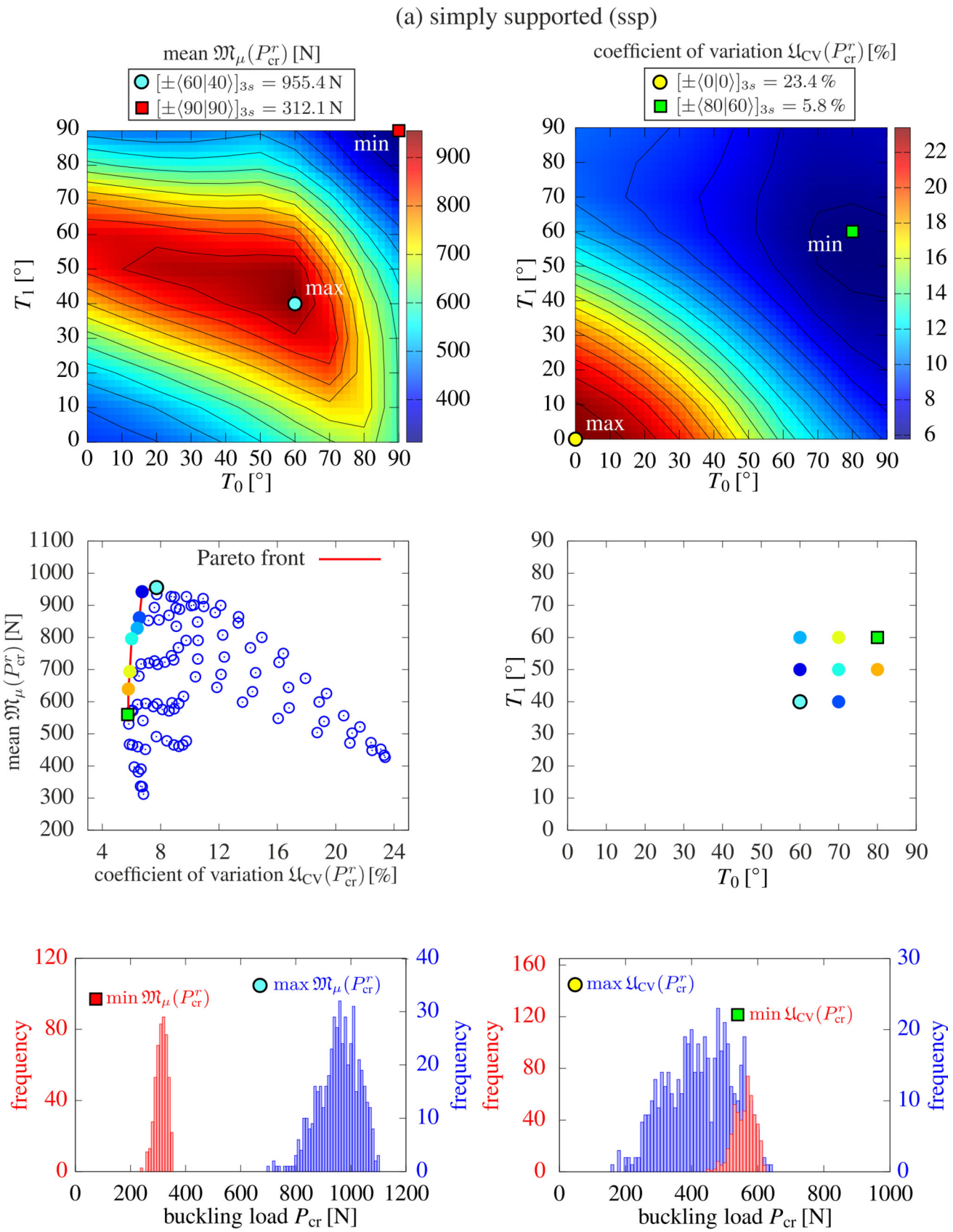

Fig. 23 VAT composite panel $[\pm\langle T_0|T_1\rangle]_{3s}$ with ssp boundary conditions under random geometric imperfections for $\ell_c = 750\,\mathrm{mm}$: contour plots of mean and CV of the buckling load P_{cr} via the fiber orientation angles T_0, T_1 (top), Pareto front with corresponding design points (middle) and corresponding histograms to the extreme values (bottom)

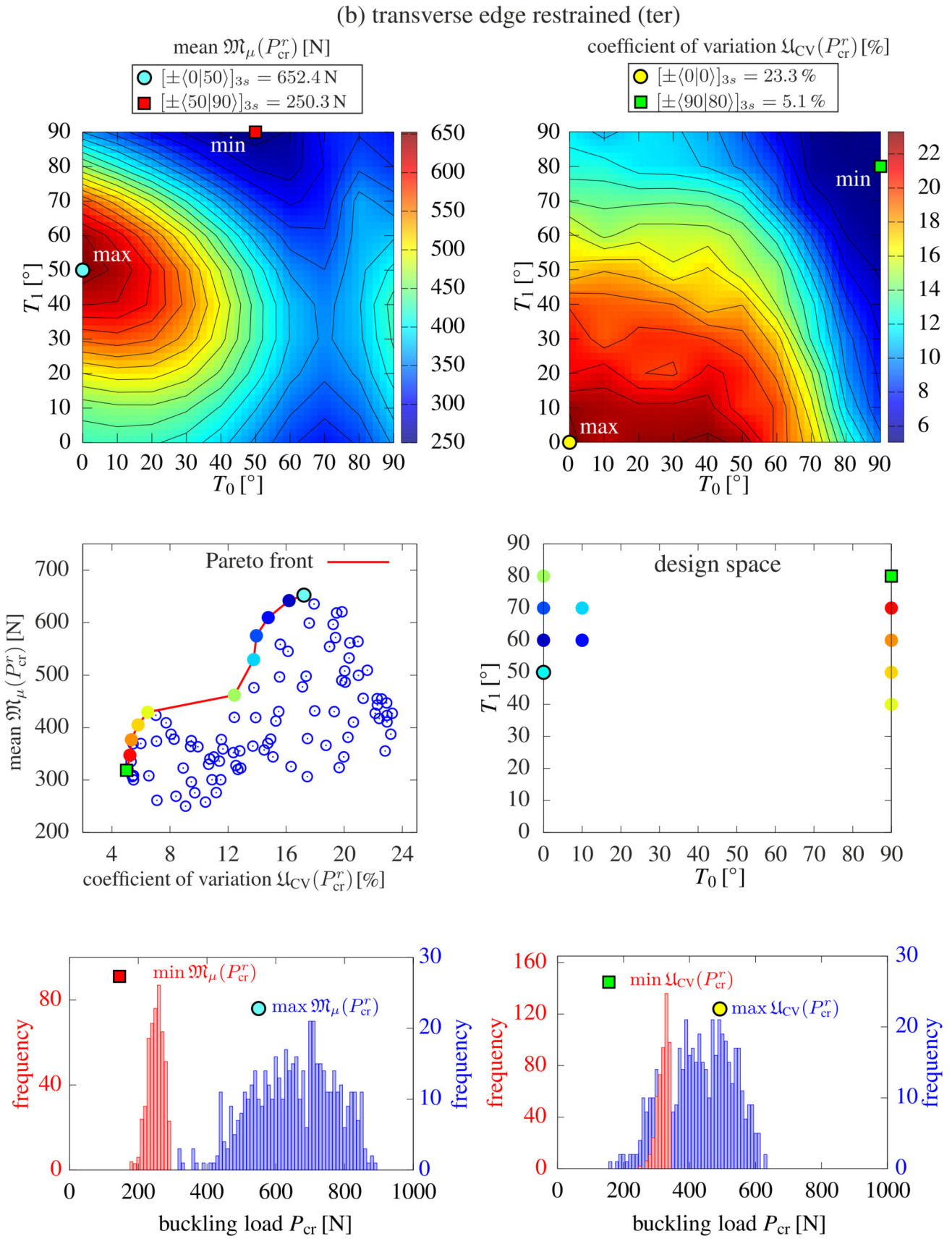

Fig. 24 VAT composite plate $[\pm\langle T_0|T_1\rangle]_{3s}$ with ter boundary conditions under random geometric imperfections for $\ell_c = 750$ mm: contour plots of mean and CV of the buckling load $P_{\rm cr}$ via the fiber orientation angles T_0, T_1 (top), Pareto front with corresponding design points (middle) and corresponding histograms to the extreme values (bottom)

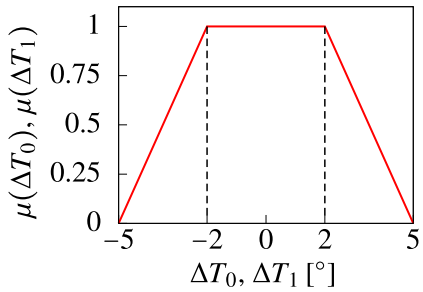

Fig. 25 Variation of the fiber orientation angle ΔT_0 and ΔT_1 defined by fuzzy variables

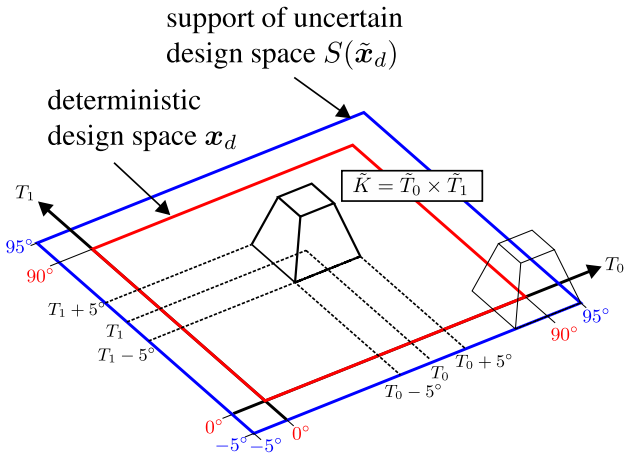

Fig. 26 Deterministic design space and support of the uncertain design space as the ANN training space

be observed near the inflection points. Consequently, low memberships are assigned to values around 5°. It is assumed that the angle variations are constant at each location of the panel. This means, the fuzzy variables defined in Eq. (50) do not change across the panel. This assumption implies the homogeneity of the fuzzy fiber path (fuzzy function). However, distinct fuzzy variables for the fiber angle variation can be defined at specific locations, such as near the inflection points, where higher variations are typically expected. Thus, the uncertainty quantification can be improved and warrants further investigation.

The fuzzy trapezoidal numbers defined in Eq. (50) are added on each point of the deterministic design space $\boldsymbol{x}_d = \{T_0, T_1\} \in \mathcal{D}$ with $T_0, T_1 = [0, 90]$

$$\begin{aligned} \tilde{T}_0 &= T_0 + \Delta\tilde{T}_0 \\ \tilde{T}_1 &= T_1 + \Delta\tilde{T}_1. \end{aligned} \tag{51}$$

Thus, at each point, a Cartesian product $\tilde{K} = \tilde{T}_0 \times \tilde{T}_1$ can be formed, representing a three-dimensional trapezoid as depicted in Fig. 26. This results in an uncertain design space $\tilde{\boldsymbol{x}}_d = \tilde{T}_0, \tilde{T}_1$, where the support $S(\tilde{T}_0), S(\tilde{T}_1) = [-5°, 95°]$ constitutes the training space for the ANN.

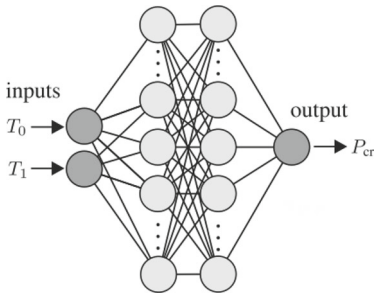

Fig. 27 ANN architecture

A fully connected feedforward neural network is constructed using MATLAB to learn the relationships between fiber orientation angles (input) and the buckling load (output). The architecture with input, output and hidden layers is depicted in Fig. 27. The two fiber orientation angles, T_0 and T_1, within the range $[-5°, 95°]$, form the input layer, normalized to the interval $[-1, 1]$. They are passed to the hidden layers and transformed back to the physical space of P_{cr} in the output layer.

To accurately predict the buckling load P_{cr}, an architecture of [5 20] with two hidden layers is selected. This topology has been proved by a previous study. For this purpose, no hyper-parameter optimization has been required. The first hidden layer comprises 5 neurons, while the second hidden layer comprises 20 neurons. The hyperbolic tangent function is chosen as the activation function for all neurons in the hidden layers. Furthermore, the Levenberg-Marquardt backpropagation algorithm is chosen as the training function, with a learning rate of 0.01. The network is trained with 2500 sample points arranged in a 50×50 regular grid with a mesh wide of approximately 2°. This equidistant sampling approach is chosen based on the UQ of the variation in fiber orientation angles, which falls within the range of ±2°. Advanced sampling techniques, such as importance sampling or Latin Hypercube sampling, are not employed in this paper. However, for optimization tasks with a larger number of design variables, which increase the dimensionality of the training space, advanced sampling methods are recommended. The design points are randomly divided into 70% for training, 15% for validation, and 15% for testing. For this purpose, no cross validation has been required.

Two separate ANNs are trained for both boundary conditions, ssp and ter. To identify the stability points in the training process, the criterion defined in Eq. (49) is applied to each sample point. Exemplary, in Fig. 28, the mean square error (mse) is depicted as the loss function via training epochs for the panel with ssp boundary conditions. The mse decreases over the training epochs, and particularly, the stable mse on the validation data indicates that the network is well-trained without overfitting. The response surfaces of the two trained ANNs for both boundary conditions are depicted in Fig. 29.

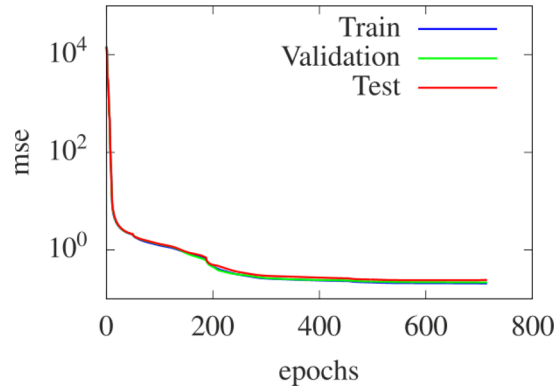

Fig. 28 Loss functions (mse) via training epochs for the VAT composite panel with ssp boundary conditions

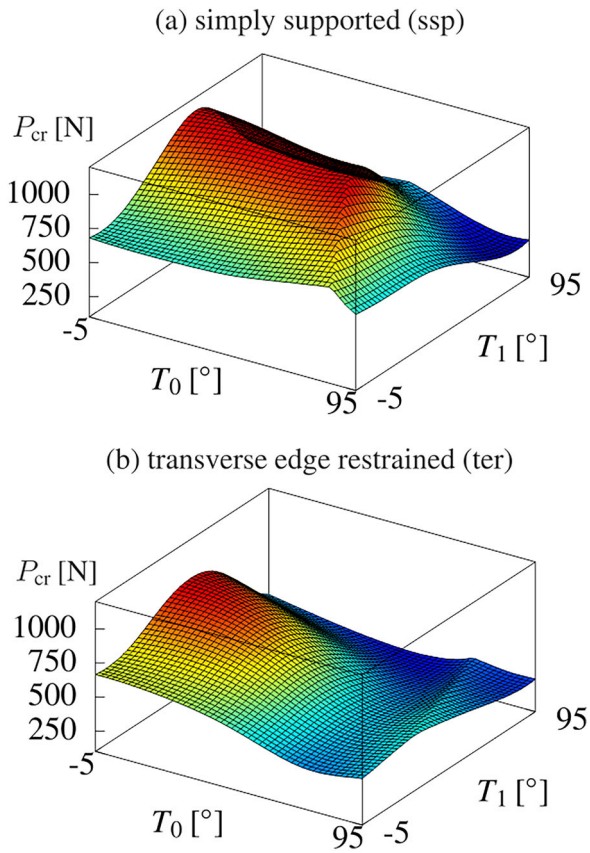

Fig. 29 Response surface of the two trained ANNs for boundary condition ssp (top) and ter (bottom)

In the response surfaces, kinks are observed, which are accurately captured by the trained ANNs.

The ANNs are employed to conduct the fuzzy analysis (ALO), as depicted in Fig. 4, within the optimization task considering epistemic uncertainty of the fiber paths. In Fig. 30 and Fig. 31, the optimization results for both boundary conditions are presented.

The trained ANNs are evaluated at 361 design points (19 × 19 grid) to determine the centroid $\mathfrak{M}_{x_S}(\tilde{P}_{\mathrm{cr}})$ (performance measure) and the area $\mathfrak{U}_A(\tilde{P}_{\mathrm{cr}})$ (robustness measure) of the fuzzy buckling load $\tilde{P}_{\mathrm{cr}}$. For this purpose, the fuzzy output variables of the buckling load $\tilde{P}_{\mathrm{cr}}$ are discretized into 10 α-levels. Utilizing the solutions from the 361 design points, contour plots, Pareto fronts, and fuzzy output variables are generated.

The Pareto fronts for both boundary conditions contain only a few valuable design points. However, the epistemic uncertainty of the fiber orientation angles can significantly influence the optimization results. This is evident in the fuzzy output variables associated with max $\mathfrak{U}_A(\tilde{P}_{\mathrm{cr}})$ in Fig. 30 and Fig. 31 (bottom). For instance, the support length $S(\tilde{P}_{\mathrm{cr}})$ of the fuzzy output variable for the panel with ssp boundary conditions is approximately 310 N, and for ter, it is 216 N. As a concluding remark on the results, it's worth noting that despite minor deviations of the fiber orientation angles, significant discrepancies in the buckling load can occur. Even with high accuracies achieved through modern manufacturing processes, the buckling load can vary significantly.

In summary, the optimal design points for panels with high levels of both robustness min $\mathfrak{U}_A$ and performance max $\mathfrak{M}_{x_S}$ compared to the deterministic optimization result max P_{cr} are presented in Table 5. It is shown, that the laminate configurations vary significantly depending on the optimization objectives. Consequently, for highly optimized VAT composite panels, it is essential to consider both aleatory and epistemic uncertainties.

5.3 Axially loaded VAT composite cylindrical shell

The proposed methods are applied to an experimental test cylinder from [44], which allows the results to be validated using experimental data.

5.3.1 FE model of the test cylinder

The cylinder was manufactured by the Dutch National Aerospace Laboratory (NLR). Photos of the test cylinder are depicted in Fig. 32. It is important to emphasize that the VAT composite test cylinder was not designed for maximum stiffness or buckling load. Instead, the primary objective of this cylinder was to conduct a feasibility study on the manufacturing method that combines parallel and shifted tows [44]. However, in this paper, optimization is performed with consideration for uncertainties, based on the experimental data from [44].

The FE model of the test cylinder is depicted in Fig. 33. Following a convergence study, a FE mesh with 140 shell elements in the circumferential direction and 60 elements in the axial direction is selected. This regular FE mesh can accurately represent the critical buckling forms. The test cylinder

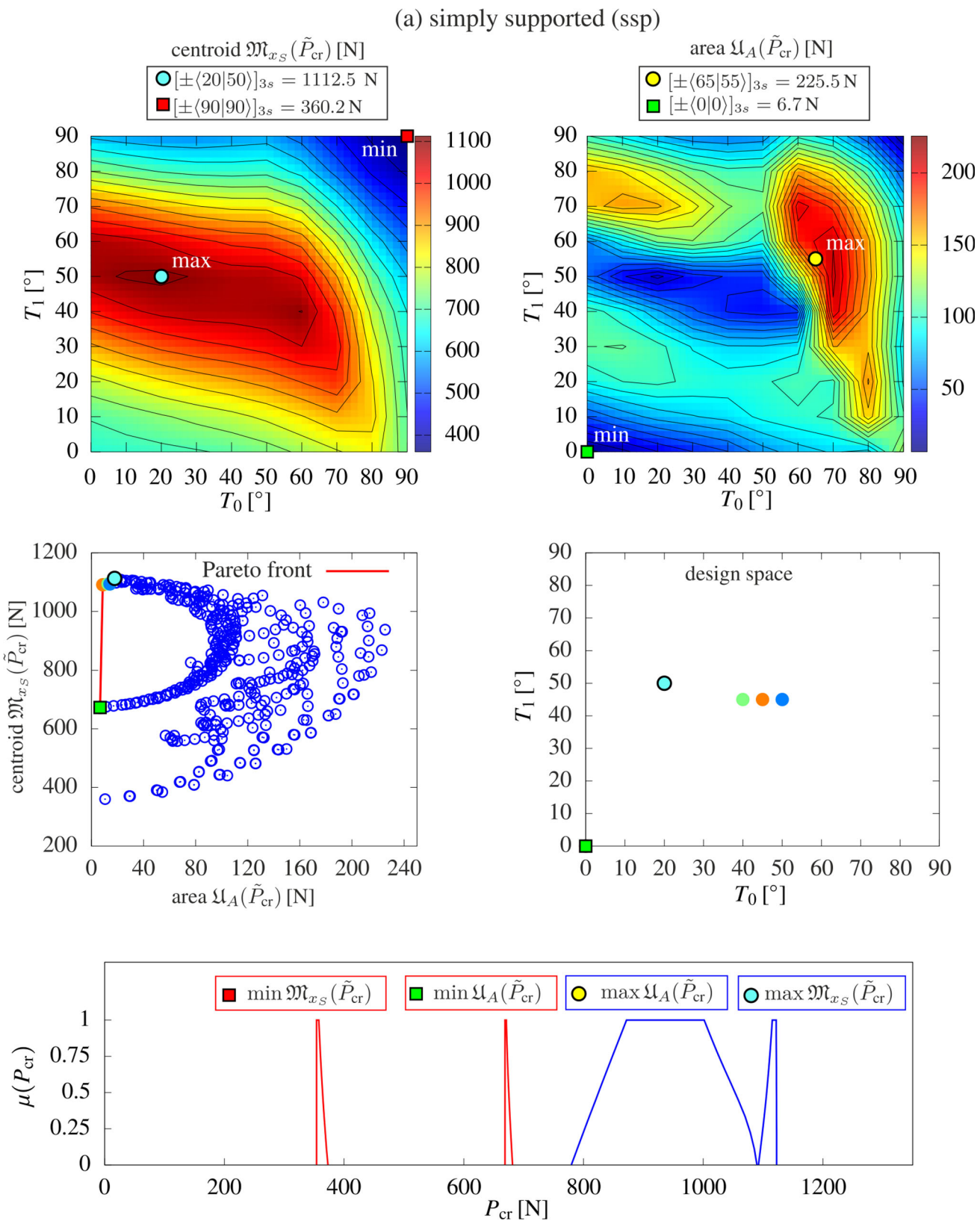

Fig. 30 VAT composite panel with ssp boundary conditions considering epistemic uncertainties of the fiber path: contour plot of centroid $\mathfrak{M}_{x_S}(\tilde{P}_{\mathrm{cr}})$ and area $\mathfrak{U}_A(\tilde{P}_{\mathrm{cr}})$ of the fuzzy buckling load P_{cr} via the fiber orientation angles T_0, T_1 (top), Pareto front with corresponding design points (middle) and corresponding fuzzy buckling loads P_{cr} to the extreme values (bottom)

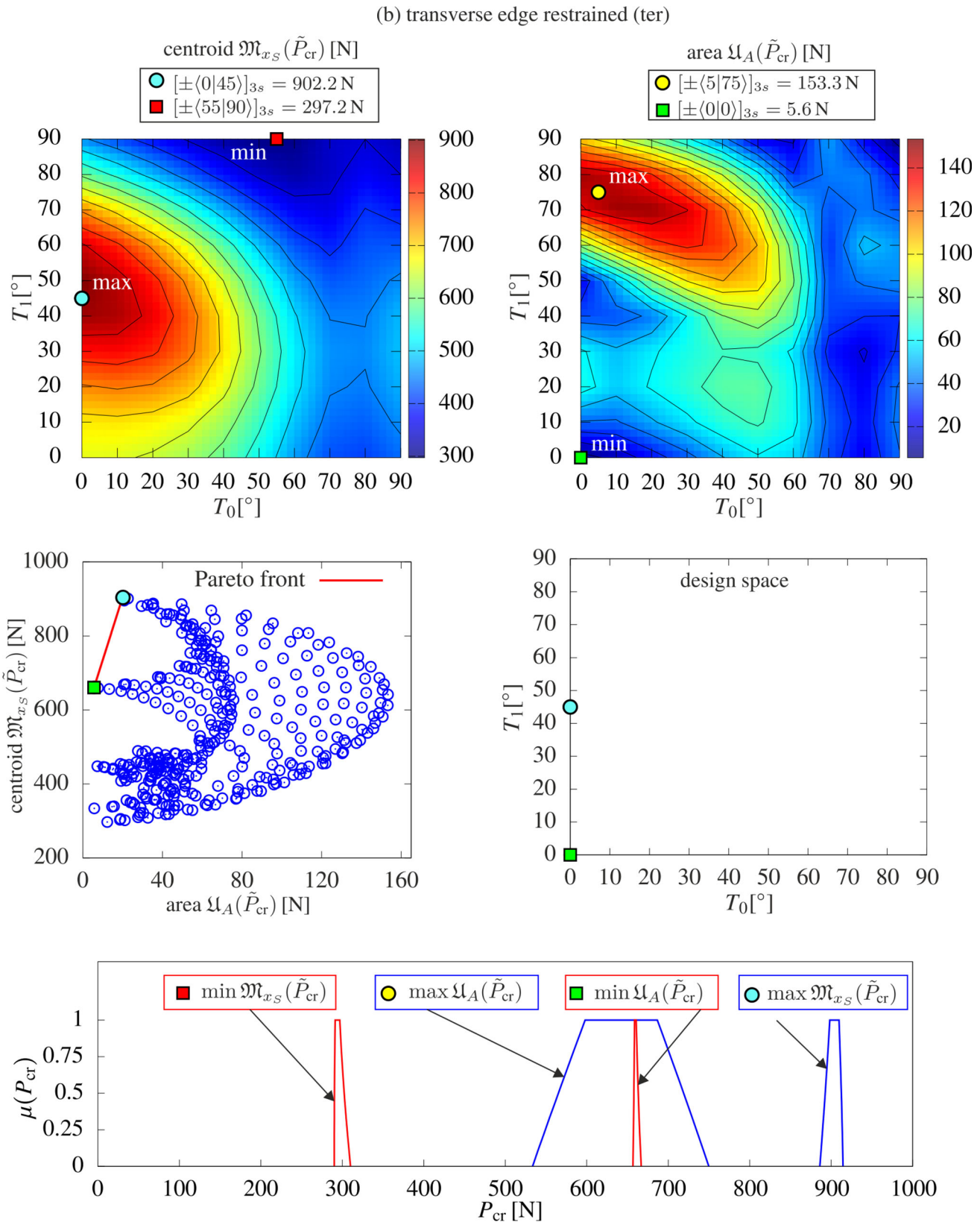

Fig. 31 VAT composite panel with ter boundary conditions considering epistemic uncertainties of the fiber path: contour plot of centroid $\mathfrak{M}_{x_S}(\tilde{P}_{\mathrm{cr}})$ and area $\mathfrak{U}_A(\tilde{P}_{\mathrm{cr}})$ of the fuzzy buckling load P_{cr} via the fiber orientation angles T_0, T_1 (top), Pareto front with corresponding design points (middle) and corresponding fuzzy buckling loads P_{cr} to the extreme values (bottom)

Table 5 VAT composite panels: optimal design points considering epistemic uncertainties

	max P_{cr}	max $\mathfrak{M}_{x_S}$	min $\mathfrak{U}_A$
ssp	$[\pm\langle 15\vert 50\rangle]_{3s}$	$[\pm\langle 20\vert 50\rangle]_{3s}$	$[\pm\langle 0\vert 0\rangle]_{3s}$
ter	$[\pm\langle 0\vert 50\rangle]_{3s}$	$[\pm\langle 0\vert 45\rangle]_{3s}$	$[\pm\langle 0\vert 0\rangle]_{3s}$

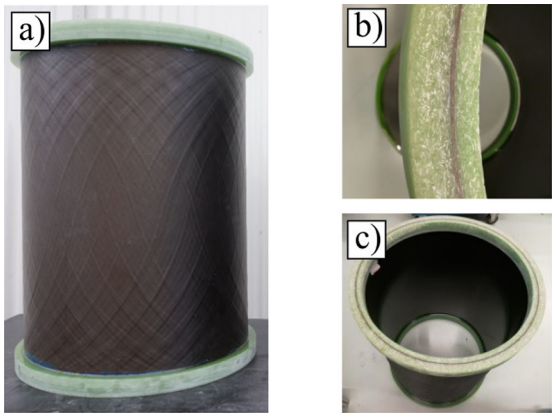

Fig. 32 Photos of the VAT composite test cylinder from [44]: a) side view, b) close-up view of potting, and c) top view

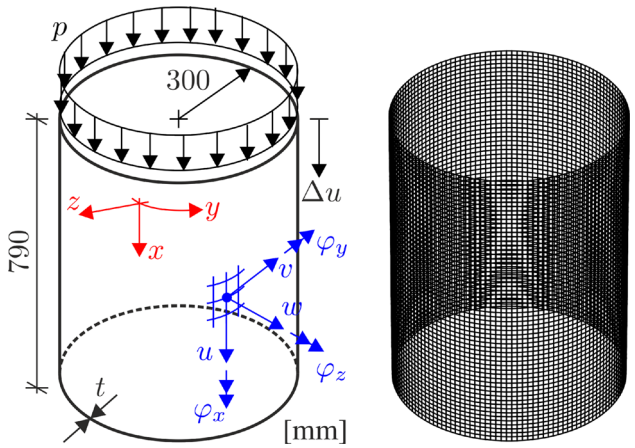

Fig. 33 FE model of the VAT composite cylindrical shell

features an epoxy resin end-potting as depicted in Fig. 32 b), enabling the application of load onto the structure. The outer thickness of the potting measures 25 mm, while the inner thickness is 15 mm. The potting covers 40 mm of the height at each end of the test cylinder. The end-potting represents a clamping and is not modeled in detail, e.g., with solid elements. Therefore, the FE model of cylinder is clamped on both edges. The boundary condition holds at the lower edge: $u = v = w = 0, \varphi_x = \varphi_y = 0$ and at the upper edge: $u = \Delta u, v = w = 0, \varphi_x = \varphi_y = 0$. Only vertical displacements of the upper nodes are allowed, where the cylinder is incrementally loaded by displacement control with $\Delta u = 0.02$ mm until a first diagonal element D_{ii} of the tangent stiffness matrix occurs. With this criterion defined in Eq. (49), the stability point is identified and each calculation is terminated within the parallelized optimization framework.

Table 6 Material properties of the AS4/8552 CFRP prepreg composite material

E_{11} [N/mm^2]	E_{22} [N/mm^2]	G_{12} [N/mm^2]	ν_{12} [−]
141 000	10 300	4 500	0.3

The cylinder is fabricated using AS4/8552 CFRP prepreg composite material, with the corresponding material parameters listed in Table 6.

The cylinder's laminate consists of 8 layers with a layup of $[\pm 45/\pm\langle T_0\vert T_1\rangle]_s$, where the two outer layers are straight fibers and the inner layers are fiber-steered plies. The fiber orientation angle of the steered layers varies along the axial direction (x') from T_0 at the midpoint of the cylinder to T_1 at the top and bottom of the cylinder. The fiber path is shifted along the circumference direction (y'), as illustrated on the unwound cylinder in Fig. 34. Using Eq. (36), the fiber orientation angles can be computed with $T_0 = -15°$ and $T_1 = -60°$. However, the introduced $x'y'$-coordinate system is rotated by 90° compared to the fiber orientation angle φ^e of the shell element, see Fig. 34. Therefore, all angles are defined based on φ^e. Thus, the fiber orientation angles of the test cylinder are specified as $T_0^e = -15° + 90° = 75°$ and $T_1^e = -15° + 90° = 75°$. The corresponding distribution of the fiber orientation angle evaluated on the FE node is depicted in Fig. 35.

The thickness of a single layer is $t = 0.181$ mm. This results in a total shell thickness of 1.448 mm, but only in the central region of the cylinder. At the ends of the cylinder, overlaps can be observed due to the shift in circumferential direction. Hence, the laminate thickness almost doubles at both ends of the cylinder. To model these overlaps, additional steered plies are incorporated into the end sections, as illustrated in Fig. 36. Alternatively, the thickness distribution can be modeled with a smooth function. However, the presented thickness build-up has been adapted from the work of [44] to compare the results. In general, the thickness distribution significantly influences the resulting buckling loads and the overall mass of the structure. Therefore, future studies should aim to quantify the uncertainties associated with the thickness build-ups.

5.3.2 Measured geometrical imperfections

Measured geometrical imperfections are applied on the FE model of the cylinder as geometric radial deviations along the z-axis in Fig. 33. In [44], measurements of geometrical imperfections are presented. The measurements are performed before the compression test using the Digital

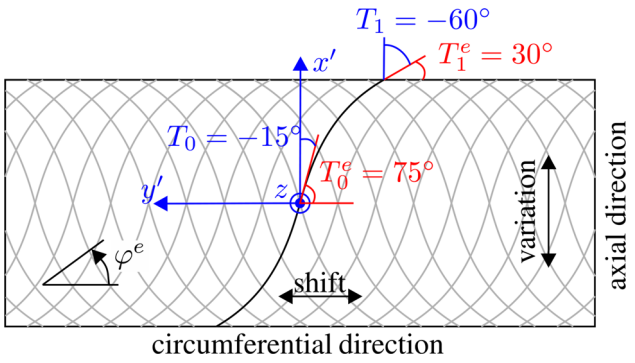

Fig. 34 Fiber path of the steered layers on the unwound cylinder

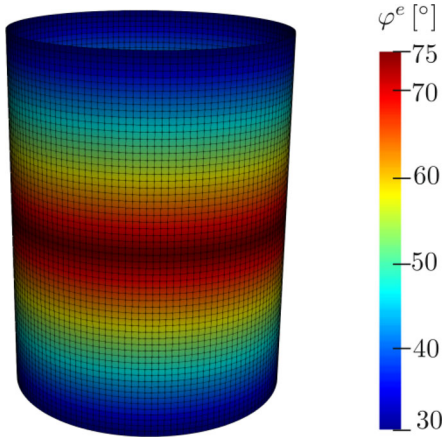

Fig. 35 Distribution of the fiber orientation angle

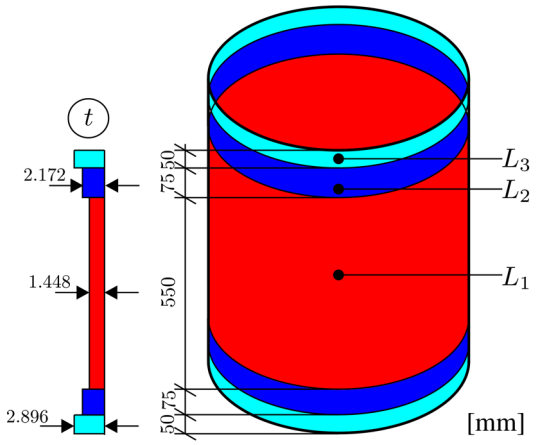

L_1: $[\pm 45/\pm\langle T_0^e|T_1^e\rangle]_s$
L_2: $[\pm 45/\pm\langle T_0^e|T_1^e\rangle/\pm\langle T_0^e|T_1^e\rangle]_s$
L_3: $[\pm 45/\pm\langle T_0^e|T_1^e\rangle/\pm\langle T_0^e|T_1^e\rangle/\pm\langle T_0^e|T_1^e\rangle]_s$

Fig. 36 Material and thickness distribution of the FE model of the VAT composite cylindrical shell

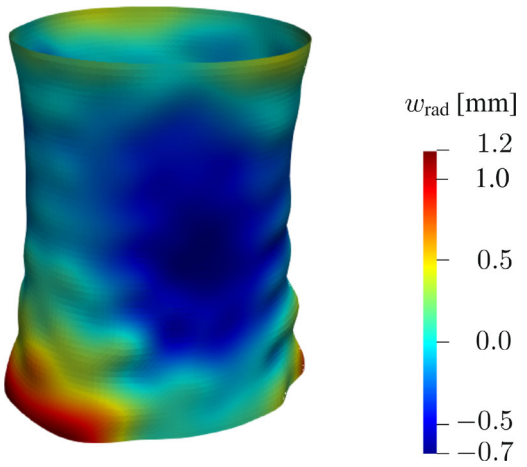

Fig. 37 Imperfect VAT composite cylindrical shell, magnified (x50)

Image Correlation (DIC) system from the outer side and a laser distance sensor from the inner side. In this paper, the imperfection data obtained from the DIC system are utilized. The geometric radial deviations are approximated with the Fourier series using the half-wave cosine formulation according to Eq. (A1) in appendix A. The corresponding Fourier coefficients are available open access in a data repository at https://doi.org/10.35097/km10c39fd3qa12kk.

The imperfect cylinder, magnified by a factor of 50, is depicted in Fig. 37 and the imperfections on the unwrapped surface are shown in Fig. 42. Positive values signify imperfections larger than the radius of the cylinder without imperfections, while negative values indicate imperfections smaller than the radius. The cylinder is deformed into an oval shape at the lower edge, where a maximum imperfection value of approximately $+1.2$ mm is observed. Within the inner area, the cylinder is curved inward with a maximum imperfection amplitude of -0.7 mm. These approximated imperfections w_{rad}, obtained through the half-wave cosine formulation, are incorporated into the FE model as geometric radial deviations from the cylinder without imperfections. Finally, it should be noted that no aleatory uncertainty is considered in this example. To quantify aleatory uncertainty from only a single measurement would not provide meaningful results. Therefore, the following optimization results are based on the measured imperfection signature. However, the influence of epistemic uncertainty in the fiber path on the optimization results is investigated.

5.3.3 Buckling analysis

Before an optimization considering uncertainties, the results of the numerical buckling analysis are validated with the experimental buckling tests obtained by Labans et al. [44]. The experimental and numerical load-displacement curves of the cylinder are depicted in Fig. 38. Therein, the numerical

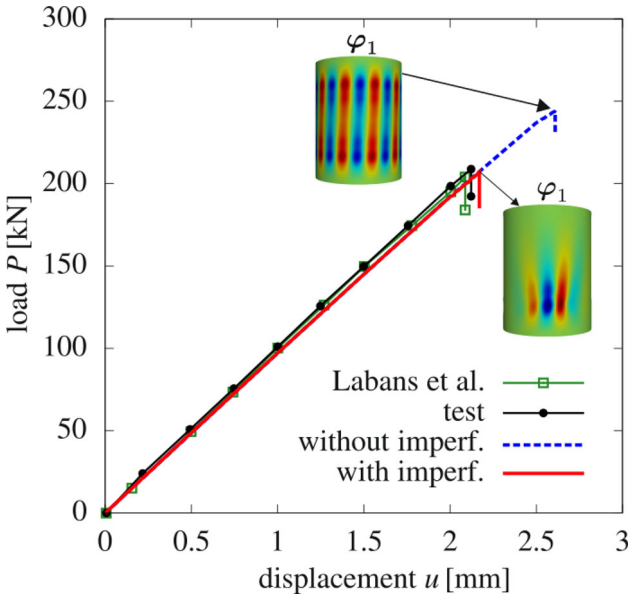

Fig. 38 Load-displacement curves of the VAT composite cylinder

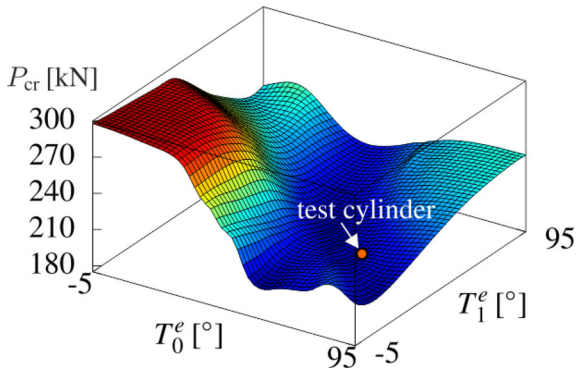

Fig. 39 Response surface of the trained ANN for the VAT composite cylindrical shell

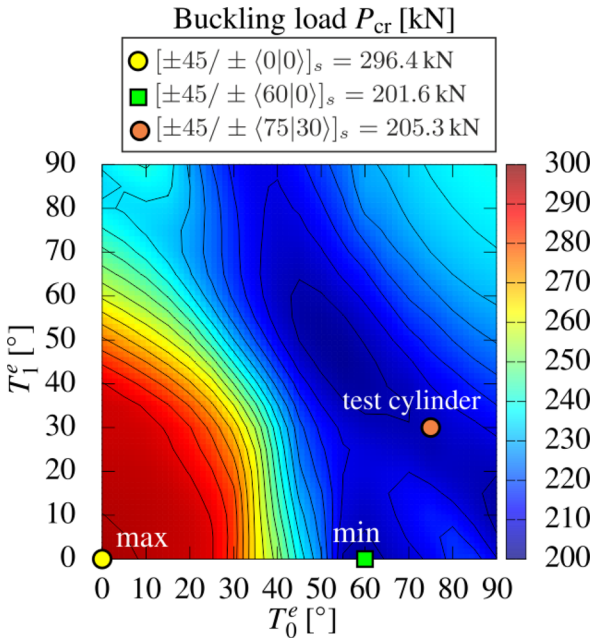

Fig. 40 Deterministic buckling optimization of the VAT composite cylindrical shell

results from [44] (green line) are also provided. The test cylinder is loaded in compression several times. In Fig. 38, the median experimental load-displacement curve is indicated by the black line, labeled as "test". The median experimental buckling load is $P_{cr} = 208\,\text{kN}$ at the critical displacement $u_{cr} = 2.2\,\text{mm}$. The standard deviation of the experimental buckling load is 1.6 kN based on 8 compression tests [44]. A linear buckling analysis of the cylinder without imperfections reveals a buckling load of $P_{cr} = 249\,\text{kN}$, which results in a knockdown factor of $208\,\text{kN}/249\,\text{kN} = 0.835$. The numerical load-displacement curves of the cylinder, both without imperfections (blue dashed line) and with imperfections (red line), are calculated, presenting the first eigenvector $\boldsymbol{\varphi}_1$ at the stability point. The nonlinear buckling load of the imperfect cylinder is $P_{cr} = 207\,\text{kN}$ at the critical displacement $u_{cr} = 2.17\,\text{mm}$. This agrees with the experimental and numerical results reported by Labans et al. [44].

5.3.4 Optimization

The classical buckling optimization with deterministic design variables according to Eq. (27) and the optimization under epistemic uncertainty given by Eq. (31) are performed based on an ANN, which is trained on the support of the uncertain design space as depicted in Fig. 26. The fiber orientation angles T_0^e and T_1^e are the ANN inputs, which are bounded within the range $[-5°, 95°]$. As in the panel example in Sect. 5.2.3, the same ANN architecture [5 20] and training settings are used. This topology has also been proved by a previous study without a hyperparameter optimization. The design points are randomly divided into 70% for training, 15% for validation, and 15% for testing. For this purpose, no cross validation has been required.

The ANN is trained on a fine grid of size 50×50, comprising 2500 sample points, to ensure accurate optimization results considering uncertain fiber paths. At each sample point, a nonlinear buckling analysis is conducted using the criterion in Eq. (49) to terminate the calculation at the stability point during the training process. The response surface of the trained ANN is depicted in Fig. 39, where the solution of the test cylinder $[\pm 45/\pm\langle 75|30\rangle]_s$ is marked.

Significant gradients can be observed, indicating the need for optimization under uncertainty. The investigated cylinder has significant potential to enhance the buckling load for specific fiber orientation angles. As stated in [44], the cylinder was not designed for maximum stiffness or buckling load.

Table 7 VAT composite cylindrical shell: optimal design points considering epistemic uncertainties

$\max P_{\mathrm{cr}}$	$\max \mathfrak{M}_{x_S}$	$\min \mathfrak{U}_A$
$[\pm 45/\pm\langle 0\vert 0\rangle]_s$	$[\pm 45/\pm\langle 0\vert 0\rangle]_s$	$[\pm 45/\pm\langle 0\vert 30\rangle]_s$

A deterministic optimization is conducted utilizing the ANN solutions. For this purpose, the ANN is evaluated at 361 design points (19×19 grid) for T_0^e and T_1^e in the range $[0°, 90°]$. The results for the maximum and minimum buckling load are depicted in Fig. 40. Additionally, it shows the ANN result of the test cylinder with a buckling load of $P_{\mathrm{cr}} = 205.3\,\mathrm{kN}$, which closely correlates with the FE solution of $P_{\mathrm{cr}} = 207\,\mathrm{kN}$ presented in Sect. 5.3.3. In summary, the buckling load can be increased up to $P_{\mathrm{cr}} = 296\,\mathrm{kN}$.

Finally, the ANN is used to perform an optimization taking into account epistemic uncertainty of the fiber path. The variations of the fiber orientation angles are quantified with the same fuzzy trapezoidal numbers defined in Eq. (50) and depicted in Fig. 25. No investigations are conducted for the test cylinder regarding deviations in the fiber path. Therefore, the uncertainty quantification of the fiber path is performed based on the results in [42] as described in Sect. 5.2.3.

In Fig. 41, the results of the optimization under uncertainty are depicted. The centroid $\mathfrak{M}_{x_S}(\tilde{P}_{\mathrm{cr}})$ (performance measure) and the area $\mathfrak{U}_A(\tilde{P}_{\mathrm{cr}})$ (robustness measure) of the fuzzy buckling load $\tilde{P}_{\mathrm{cr}}$ is evaluated using the trained ANN at 361 design points (19×19 grid), where the fuzzy input and output variables are discretized into 10 α-levels. In Fig. 41, contour plots, the Pareto front, and fuzzy output variables of the extreme values are provided. The Pareto front contains only a few design points and shows no conflict between the two objectives. Furthermore, Fig. 41 includes the result of the test cylinder as one feasible solution. It can be observed that the performance $\mathfrak{M}_{x_S}$ of the test cylinder is low, whereas the robustness $\mathfrak{U}_A$ is quite high. This illustrates how taking into account of uncertainties in an optimization approach can lead to additional statements about the structure. Optimal design points compared to the classical (deterministic) optimization result $\max P_{\mathrm{cr}}$ are summarized in Table 7. The laminate configurations are quite similar. However, for some configuration the robustness is very low. In Fig. 41 (bottom), the fuzzy buckling load assigned to $\max \mathfrak{U}_A$ shows a large support length $S(\tilde{P}_{\mathrm{cr}})$ of approximately 45 kN. Even small deviations in the fiber path here also result in significant differences in the buckling loads. This emphasizes the importance of accounting for uncertainty in the optimization process of VAT composite shells.

6 Conclusions

This paper proposes a methodology to consider aleatory and epistemic uncertainties within a multi-objective optimization framework for tow-steered composite shells. An optimization under uncertainties requires a considerable amount of computational effort, for which a multi-loop computational model based on neural networks is presented. The robustness and performance of a VAT composite structure are discussed based on the IRMs of the uncertain output quantities such as mean value, coefficient of variation, area, and centroid of a fuzzy variable. The conflicts between these objectives are shown by Pareto fronts. In the first example, random geometric imperfections are applied on a VAT composite panel. It is demonstrated that conflicts may occur depending on the boundary conditions. The performance, represented by the mean value of the buckling load, can only be enhanced at the expense of decreased robustness, indicated by an increase in the variation of the buckling load. Such results have to be considered in a decision-making process for highly optimized structures. Only then can an appropriate level of safety be guaranteed.

One highlight of the paper is the uncertain fiber path definition with fuzzy functions to consider the deviations of the fiber path, for which usually only a few measurements are available. This epistemic uncertainty of the fiber orientation angles can significantly influence the optimization results. It's worth noting that despite minor deviations of the fiber orientation angles, significant discrepancies in the buckling load can occur, even with high accuracies achieved through modern manufacturing processes. That is further confirmed by the second example: the VAT composite cylindrical shell. This example involves a test cylinder for which imperfection measurements are available and provided in the paper to replicate the results. It serves as a demonstration of the methods applied to manufactured structures.

The proposed approach aims to initiate a paradigm shift moving away from the classical optimization with deterministic design variables of aerospace structures. This shift contributes to paving the way for the next generation of aircraft to be lighter and more sustainable. To maintain or enhance safety standards, it is absolutely essential to account for the inherent aleatory and epistemic uncertainties in numerical design optimization. Hence, future work should focus on how to address uncertainties in advanced modeling and design tool, extending beyond VAT composite structures. New ideas for further research and possible applications of the proposed methods can be summarized as follows:

- Improved uncertain fiber path definition with respect to the manufacturing process (AFP, CTS)

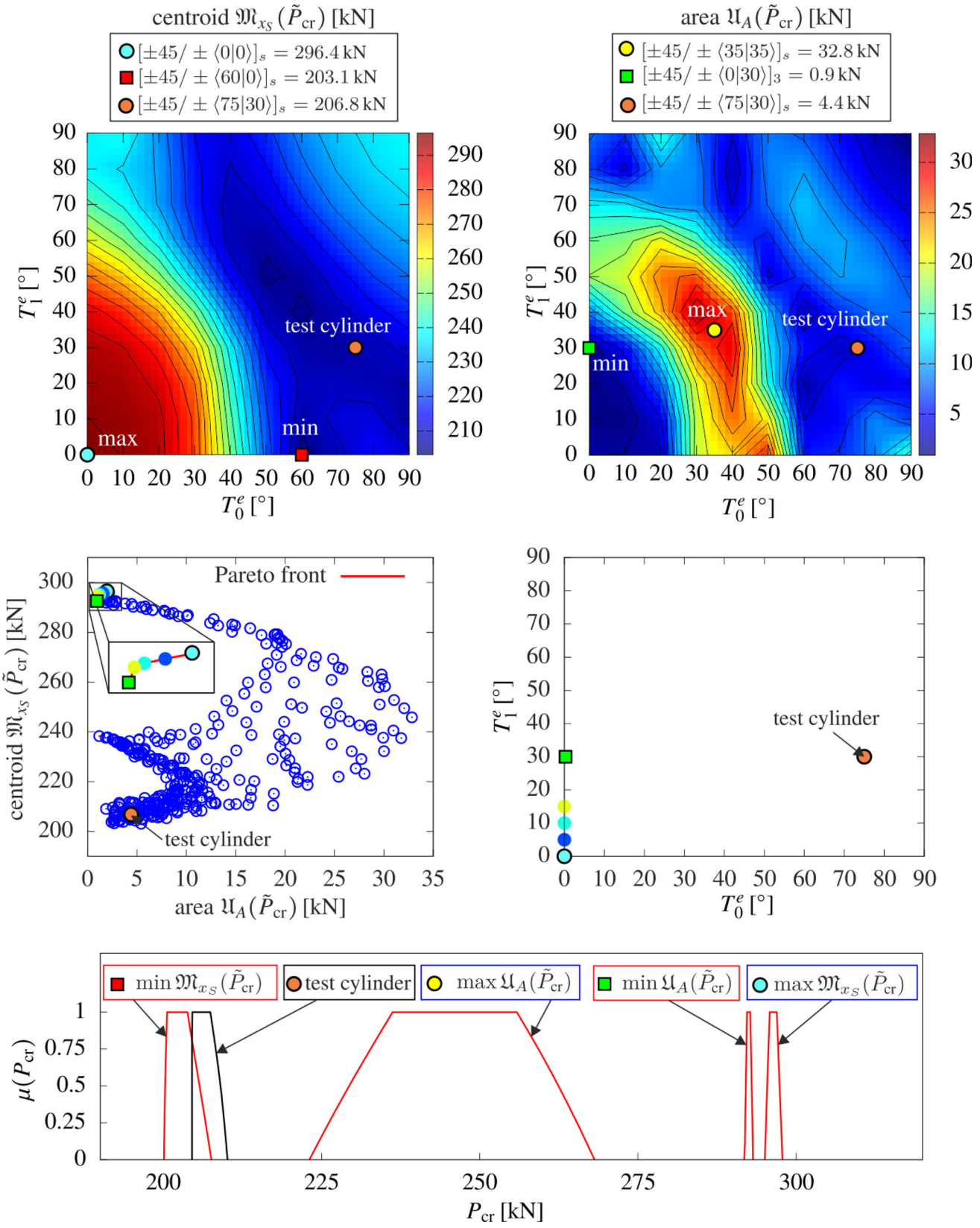

Fig. 41 VAT composite cylindrical shell considering epistemic uncertainties of the fiber path: contour plot of centroid $\mathfrak{M}_{x_S}(\tilde{P}_{\mathrm{cr}})$ and area $\mathfrak{U}_A(\tilde{P}_{\mathrm{cr}})$ of the fuzzy buckling load P_{cr} via the fiber orientation angles T_0^e, T_1^e (top), Pareto front with corresponding design points (middle) and corresponding fuzzy buckling loads P_{cr} to the extreme values and the test cylinder (bottom)

- Additional uncertainty quantification of thickness distributions and overlaps from tow-steering
- Optimization under uncertainty with regard to the post-buckling behavior
- Exploration of various boundary conditions and load cases to identify potential conflicts between robustness and performance objectives, especially for cylindrical shells
- Extension to polymorphic uncertainty modeling to consider aleatory and epistemic uncertainty simultaneously
- Development of specific surrogate models for buckling design optimization
- Optimization under polymorphic uncertainties in real tow-steered structures with significantly higher number of degrees of freedom.
- Application to various structures, such as stiffened panels, conical shells, large-scale structures, morphing adaptive structures, etc.

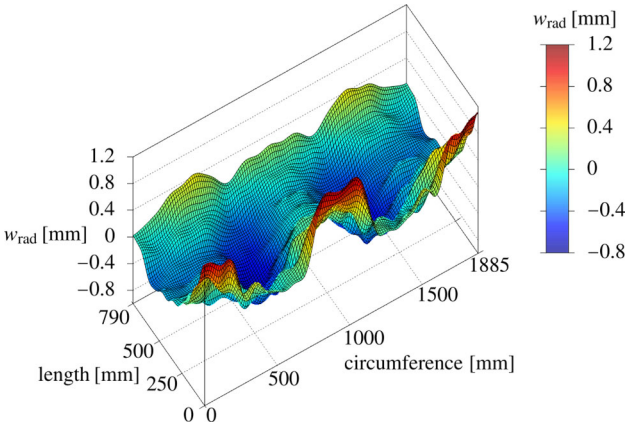

Fig. 42 Measured geometrical imperfection on the unwrapped surface of the VAT composite cylindrical shell

Appendix A: Fourier coefficients of measured geometric imperfections of the VAT composite shell

The measured geometric imperfections of the VAT composite cylindrical shell, as presented in Sect. 5.3, are approximated using the half-wave cosine formulation, defined as follows [7, 43]:

$$w_{\mathrm{rad}}(x,y) = \sum_{m=0}^{N_m}\sum_{n=0}^{N_n} \cos\left(\frac{m\pi x}{L}\right) \left[A_{mn}\cos\left(\frac{n\cdot y}{R}\right) + B_{mn}\sin\left(\frac{n\cdot y}{R}\right)\right], \tag{A1}$$

where $w_{\mathrm{rad}}(x,y)$ represents the geometric deviations in the radial direction of nodes, depending on the coordinates on the shell surface in the axial (x) and circumferential (y) directions. R denotes the radius and L the length of the cylinder. Moreover, A_{mn} and B_{mn} denote the Fourier coefficients for m half waves in the axial direction and n full waves in the circumferential direction. These coefficients can be calculated as follows:

$$A_{mn} = \frac{2\alpha}{\pi L}\int_0^{2\pi R}\int_0^{L} \bar{w}_{\mathrm{rad}}(x,y)\cos\left(\frac{m\pi x}{L}\right)\cos\left(\frac{n\cdot y}{R}\right)dx\,dy \tag{A2}$$

$$B_{mn} = \frac{2\alpha}{\pi L}\int_0^{2\pi R}\int_0^{L} \bar{w}_{\mathrm{rad}}(x,y)\cos\left(\frac{m\pi x}{L}\right)\sin\left(\frac{n\cdot y}{R}\right)dx\,dy, \tag{A3}$$

where $\bar{w}_{\mathrm{rad}}(x,y)$ are measured geometric imperfections and α is a numerical substitutor defined with Boolean operations

$$\alpha = 1 \quad \text{if } m = 0 \text{ and } n = 0 \tag{A4}$$

$$\alpha = 2 \quad \text{if } m > 0 \text{ or } n > 0 \tag{A5}$$

$$\alpha = 4 \quad \text{if } m > 0 \text{ and } n > 0. \tag{A6}$$

The integrals in Eq. (A3) are solved using the trapezoidal rule. Figure 42 depicts the geometric imperfection on the unwrapped surface of the investigated test cylinder.

The test cylinder measures $L = 790\,\mathrm{mm}$ in length and has a radius of $R = 300\,\mathrm{mm}$. To reproduce its geometric imperfections, the Fourier coefficients A_{mn} and B_{mn} of the half-wave cosine representation in Eq. (A1) are available open access in a data repository at https://doi.org/10.35097/km10c39fd3qa12kk.

Acknowledgements The initial stages of the presented paper were developed during a research stay of the first author at the Faculty of Aerospace Engineering of Delft University of Technology (TU Delft). The authors are grateful to the Karlsruhe House of Young Scientists (KHYS) for funding the research stay. The second author would like to acknowledge the funding by the European Union (ERC Advanced Grant, NABUCCO, project number 101053309). Views and opinions expressed are however those of the authors only and do not necessarily reflect those of the European Union or the European Research Council Executive Agency. Neither the European Union nor the granting authority can be held responsible for them. The first author gratefully acknowledges the financial support provided by the Deutsche Forschungsgemeinschaft (DFG, German Research Foundation) under project number 511267658.

Funding Open Access funding enabled and organized by Projekt DEAL.

Data availability The Fourier coefficients of the geometric imperfection of the VAT composite cylindrical shell are available open access in the central repository of the KIT at https://doi.org/10.35097/km10c39fd3qa12kk.

References

1. Aragh BS, Farahani EB, Xu BX, H G, Mansur WJ (2021) Manufacturable insight into modelling and design considerations in fibre-steered composite laminates: state of the art and perspective. Comput Methods Appl Mech Eng 379:113752. https://doi.org/10.1016/j.cma.2021.113752
2. Ayodele IO, Wehbe R, Brasington A, Tatting BF, Harik R (2021) Characterization of steered fiber laminates: perspectives and a survey of the state of the art on principal considerations. Comp Part C Open Access 4:100118. https://doi.org/10.1016/j.jcomc.2021.100118
3. Beer M (2002) Fuzziness und Fuzzy-Zufälligkeit bei der Sicherheitsbeurteilung von Tragwerken. H.5. Lehrstuhl für Statik, TU Dresden
4. Beer M, Ferson S, Kreinovich V (2013) Imprecise probabilities in engineering analyses. Mech Syst Signal Process 37(1):4–29. https://doi.org/10.1016/j.ymssp.2013.01.024
5. Beer M, Liebscher M (2008) Designing robust structures - a nonlinear simulation based approach. Comput Struct 86(10):1102–1122. https://doi.org/10.1016/j.compstruc.2007.05.037
6. Blom AW (2010) Structural performance of fiber-placed,variable-stiffness composite conicaland cylindrical shells. PhD thesis, Faculty of Aerospace Engineering, TU Delft
7. Böhm M, Schaumann P (2022) Stochastic modeling of geometric imperfections for buckling analysis of suction buckets. J Phys Conf Ser 2362(1):012007. https://doi.org/10.1088/1742-6596/2362/1/012007
8. Bre F, Fachinotti VD (2017) A computational multi-objective optimization method to improve energy efficiency and thermal comfort in dwellings. Energy Build 154:283–294. https://doi.org/10.1016/j.enbuild.2017.08.002
9. Brooks TR, Martins JRRA, Kennedy GJ (2019) High-fidelity aerostructural optimization of tow-steered composite wings. J Fluids Struct 88:122–147. https://doi.org/10.1016/j.jfluidstructs.2019.04.005
10. Böttcher M, Graf W, Kaliske M (2023) Designing structures with polymorphic uncertainty: enhanced decision making using information reduction measures to quantify robustness. PAMM 23(4):e202300289. https://doi.org/10.1002/pamm.202300289
11. Deb K, Gupta H (2006) Introducing robustness in multi-objective optimization. Evol Comput 14(4):463–494. https://doi.org/10.1162/evco.2006.14.4.463
12. Díaz J, Fagiano C, Abdalla MM, Gürdal Z, Hernández S (2012) A study of interlaminar stresses in variable stiffness plates. Comp Struct 94(3):1192–1199. https://doi.org/10.1016/j.compstruct.2011.10.016
13. Faes M, Fina M, Lauff C, Valdebenito MA, Wagner W, Freitag S (2022) Bounding the first excursion probability of stochastic oscillators under randomness and imprecision. In: International conference on noise and vibration engineering (ISMA), pp 4716–4722, 12–14 Sept 2022, Leuven, Belgium
14. Faes M, Fina M, Valdebenito MA, Lauff C, Wagner W, Freitag S, Beer M (2022) Bounding failure probabilities in imprecise stochastic FE models. In: Beer M, Zio E, Phoon K-K, Ayyub BM (eds) Proceedings of the 8th international symposium on reliability engineering and risk management (ISRERM), 4–7 Sept 2022, Hannover, Germany. Research Publishing. https://doi.org/10.3850/978-981-18-5184-1_MS-15-141-cd
15. Faes M, Moens D (2017) Identification and quantification of spatial interval uncertainty in numerical models. Comput Struct 192:16–33. https://doi.org/10.1016/j.compstruc.2017.07.006
16. Faes M, Moens D (2020) Recent trends in the modeling and quantification of non-probabilistic uncertainty. Arch Comput Methods Eng 27(3):633–671. https://doi.org/10.1007/s11831-019-09327-x
17. Faes M, Valdebenito MA (2020) Fully decoupled reliability-based design optimization of structural systems subject to uncertain loads. Comput Methods Appl Mech Eng 371:113313. https://doi.org/10.1016/j.cma.2020.113313
18. Fina M (2020) Polymorphe Unschärfemodellierung in der nichtlinearen Strukturmechanik – Stabilität von Schalentragwerken, räumliche Variabilität und Metamodellierung. Dissertation, Institut für Baustatik, Karlsruher Institut für Technologie, ISBN: 978–3–935322–27–0. https://doi.org/10.5445/IR/1000129960
19. Fina M, Faes M, Valdebenito MA, Wagner W, Broggi M, Beer M, Freitag S (2022) Estimation of second-order statistics of buckling loads applying linear and nonlinear analysis. In: Beer M, Zio E, Phoon K-K, Ayyub BM, (eds) Proceedings of the 8th international symposium on reliability engineering and risk management (ISRERM), 4–7 Sept 2022, Hannover, Germany. Research Publishing. https://doi.org/10.3850/978-981-18-5184-1_MS-15-145-cd
20. Fina M, Faes M, Valdebenito MA, Wagner W, Broggi M, Beer M, Freitag S (2023) Uncertainty quantification of buckling loads of thin and slender structures applying linear and nonlinear analysis. In: 14th International conference on applications of statistics and probability in civil engineering (ICASP14), 09–13 July 2023, Dublin, Ireland
21. Fina M, Lauff C, Faes M, Valdebenito MA, Wagner W, Freitag S (2023) Bounding imprecise failure probabilities in structural mechanics based on maximum standard deviation. Struct Safety 101:102293. https://doi.org/10.1016/j.strusafe.2022.102293
22. Fina M, Lauff C, Wagner W (2022) Optimal shell design with polymorphic uncertain parameters. In: Beer M, Zio E, Phoon K-K, Ayyub BM, (eds), Proceedings of the 8th international symposium on reliability engineering and risk management (ISRERM), 4–7 Sept 2022, Hannover, Germany. Research Publishing. https://doi.org/10.3850/978-981-18-5184-1_MS-12-019-cd
23. Fina M, Panther L, Weber P, Wagner W (2021) Shell buckling with polymorphic uncertain surface imperfections and sensitivity analysis. ASCE-ASME J Risk Uncertain Eng Syst Part B Mech Eng 7(2). https://doi.org/10.1115/1.4050165
24. Fina M, Schietzold FN, Heinzig S, Freitag S, Graf W, Kaliske M (2024) Incorporation of non-gaussian shell imperfections by nataf transformation in efficient random field simulation. In: ESREL 2024 collection of extended abstracts, 23–27 June 2014, Cracow, Poland. Polish Safety and Reliability Association
25. Fina M, Schweizer M, Wagner W, Freitag S (2024) Dynamische Tragwerksanalyse von Fußgängerbrücken mit unscharfen Parametern. In: Oesterle B, Bögle A, Weber W, Striefler L, (eds) Berichte der Fachtagung Baustatik–Baupraxis 15, pp 629–636, 04–05 Mar 2024, Hamburg, Germany

26. Fina M, Wagner W, Graf W (2023) On polymorphic uncertainty modeling in shell buckling. Computer-Aided Civil and Infrastructure Engineering 38(18):2632–2647. https://doi.org/10.1111/mice.13054
27. Fina M, Weber P, Wagner W (2019) A fuzzy stochastic correlation model for geometric imperfections of cylindrical shells. In: 13th International conference on applications of statistics and probability in civil engineering (ICASP13), 26–30 May 2019, Seoul, South Korea. https://doi.org/10.22725/ICASP13.479
28. Fina M, Weber P, Wagner W (2019) Modeling of aleatory and epistemic uncertainties in probabilistic design of cylindrical shells. In: Beer M, Zio E (eds) Proceedings of the 29th European safety and reliability conference (ESREL), 22–26 Sept 2019, Hannover, Germany. https://doi.org/10.3850/978-981-11-2724-3_0143-cd
29. Fina M, Weber P, Wagner W (2020) Polymorphic uncertainty modeling for the simulation of geometric imperfections in probabilistic design of cylindrical shells. Struct Safety 82:101894. https://doi.org/10.1016/j.strusafe.2019.101894
30. Freitag S, Edler P, Kremer K, Meschke G (2020) Multilevel surrogate modeling approach for optimization problems with polymorphic uncertain parameters. Int J Approx Reason 119:81–91. https://doi.org/10.1016/j.ijar.2019.12.015
31. Graf W, Götz M, Kaliske M (2014) Structural design with polymorphic uncertainty models. In: 6th International conference on reliable engineering computing, Chicago
32. Graf W, Götz M, Kaliske M (2015) Analysis of dynamical processes under consideration of polymorphic uncertainty. Struct Safety 52:194–201. https://doi.org/10.1016/j.strusafe.2014.09.003
33. Groh RMJ, Weaver PM (2014) Buckling analysis of variable angle tow, variable thickness panels with transverse shear effects. Comp Struct 107:482–493. https://doi.org/10.1016/j.compstruct.2013.08.025
34. Groh RMJ, Wu KC (2022) Nonlinear buckling and postbuckling analysis of tow-steered composite cylinders with cutouts. AIAA J 60(9):5533–5546. https://doi.org/10.2514/1.J061755
35. Götz M (2017) Numerische Entwurfmethoden unter Berücksichtigung polymorpher Unschärfe – Aspekte zeitlicher und räumlicher Abhängigkeiten. H.32. Institut für Statik und Dynamik der Tragwerke, TU Dresden
36. Götz M, Graf W, Kaliske M (2016) Structural analysis with spatial varying polymorphic uncertain parameters - fuzzy fields using spectral decomposition. In Huang H, Li J, Che JZ, (eds), 6th Asian-Pacific symposium on structural reliability and its applications (APSSRA), pp 528–533, Shanghai
37. Gürdal Z, Tatting BF, Wu CK (2008) Variable stiffness composite panels: effects of stiffness variation on the in-plane and buckling response. Comp Part A Appl Sci Manuf 39(5):911–922. https://doi.org/10.1016/j.compositesa.2007.11.015
38. Heinecke F, Willberg C (2019) Manufacturing-induced imperfections in composite parts manufactured via automated fiber placement. J Comp Sci, 3(2). https://doi.org/10.3390/jcs3020056
39. Irisarri F-X, Laurin F, Leroy F-H, Maire J-F (2011) Computational strategy for multiobjective optimization of composite stiffened panels. Comp Struct 93(3):1158–1167. https://doi.org/10.1016/j.compstruct.2010.10.005
40. Kennedy J, Russell E (1995) Particle swarm optimization. In: Proceedings of ICNN'95—international conference on neural networks, pp 1942–1948. https://doi.org/10.1109/ICNN.1995.488968
41. Kim BC, Potter K, Weaver PM (2012) Continuous tow shearing for manufacturing variable angle tow composites. Comp Part A Appl Sci Manuf 43(8):1347–1356. https://doi.org/10.1016/j.compositesa.2012.02.024
42. Kim BC, Weaver PM, Potter K (2014) Manufacturing characteristics of the continuous tow shearing method for manufacturing of variable angle tow composites. Comp Part A Appl Sci Manuf 61:141–151. https://doi.org/10.1016/j.compositesa.2014.02.019
43. Kriegesmann B, Rolfes R, Hühne C, Teßmer J, Arbocz J (2010) Probabilistic design of aaxially compressed composite cylinders with geometric and loading imperfections. Int J Struct Stabil Dyn 10(04):623–644. https://doi.org/10.1142/S0219455410003658
44. Labans E, Bisagni C (2019) Buckling and free vibration study of variable and constant-stiffness cylindrical shells. Comp Struct 210:446–457. https://doi.org/10.1016/j.compstruct.2018.11.061
45. Labans E, Bisagni C, Celebi M, Tatting B, Gürdal Z, Blom-Schieber A, Rassaian M, Wanthal S (2019) Bending of composite cylindrical shells with circular cutouts: experimental validation. J Aircraft 56(4):1534–1550. https://doi.org/10.2514/1.C035247
46. Lauterbach S, Fina M, Wagner W (2018) Influence of stochastic geometric imperfections on the load-carrying behaviour of thin-walled structures using constrained random fields. Comput Mech 62(5):1107–1125. https://doi.org/10.1007/s00466-018-1554-0
47. Lincoln R, Weaver P, Pirrera A, Groh RMJ (2021) Optimisation of imperfection-insensitive continuous tow sheared rocket launch structures. In: AIAA Scitech 2021 Forum, pp 1–19. https://doi.org/10.2514/6.2021-0202
48. Lincoln RL, Weaver PM, Pirrera A, Groh RMJ (2021) Imperfection-insensitive continuous tow-sheared cylinders. Comp Struct 260:113445. https://doi.org/10.1016/j.compstruct.2020.113445
49. Lincoln RL, Weaver PM, Pirrera A, Groh RMJ (2023) Increasing reliability of axially compressed cylinders through stiffness tailoring and optimization. Philos Trans R Soc A Math Phys Eng Sci 381(2244):20220034
50. Lopes C (2009) Damage and failure of non-conventional composite laminates. PhD thesis, TU Delft, Faculteit Luchtvaart- en Ruimtevaarttechniek
51. Lozano GG, Tiwari A, Turner C, Astwood S (2016) A review on design for manufacture of variable stiffness composite laminates. Proc Inst Mech Eng Part B J Eng Manuf 230(6):981–992. https://doi.org/10.1177/0954405415600012
52. Lukaszewicz DH-JA, Ward C, Potter KD (2012) The engineering aspects of automated prepreg layup: History, present and future. Comp Part B Eng 43(3):997–1009. https://doi.org/10.1016/j.compositesb.2011.12.003
53. Madeo A, Groh RMJ, Zucco G, Weaver PM, Zagari G, Zinno R (2017) Post-buckling analysis of variable-angle tow composite plates using koiter's approach and the finite element method. Thin-Walled Struct 110:1–13. https://doi.org/10.1016/j.tws.2016.10.012
54. Mathworks (2023) Matlab. R2023b. http://www.mathworks.com,
55. Meurer A, Kriegesmann B, Dannert M, Rolfes R (2016) Probabilistic perturbation load approach for designing axially compressed cylindrical shells. Thin Walled Struct 107:648–656. https://doi.org/10.1016/j.tws.2016.07.021
56. Möller B, Beer M (2004) Fuzzy randomness—uncertainty in civil engineering and computational mechanics. Springer. https://doi.org/10.1007/978-3-662-07358-2
57. Möller B (2004) Fuzzy randomness—a contribution to imprecise probability. ZAMM J Appl Math Mech 84(10–11):754–764. https://doi.org/10.1002/zamm.200410153
58. Möller B, Graf W, Beer M (2000) Fuzzy structural analysis using α-level optimization. Comput Mech 26(6):547–565. https://doi.org/10.1007/s004660000204
59. Pagani A, Petrolo M, Sánchez-Majano AR (2023) Stochastic characterization of multiscale material uncertainties on the fibre-matrix interface stress state of composite variable stiffness plates. Int J Eng Sci 183:103787. https://doi.org/10.1016/j.ijengsci.2022.103787
60. Pannier S, Waurick M, Graf W, Kaliske M (2013) Solutions to problems with imprecise data-An engineering perspective to general-

ized uncertainty models. Mech Syst Signal Process 37(1):105–120. https://doi.org/10.1016/j.ymssp.2012.08.002
61. Pitton SF, Ricci S, Bisagni C (2019) Buckling optimization of variable stiffness cylindrical shells through artificial intelligence techniques. Comp Struct 230:111513. https://doi.org/10.1016/j.compstruct.2019.111513
62. Reuter U (2013) Ungewissheit im Bauingenieurwesen-Spezifikation, Modellierung und Berechnung. In: Jeschke S, Jakobs E-M, Dröge A (eds) Exploring uncertainty. Springer, Berlin, Heidelberg, pp 179–208. https://doi.org/10.1007/978-3-658-00897-0_8
63. Rouhi M, Ghayoor H, Hoa SV, Hojjati M (2014) Effect of structural parameters on design of variable-stiffness composite cylinders made by fiber steering. Comp Struct 118:472–481. https://doi.org/10.1016/j.compstruct.2014.08.021
64. Rouhi M, Ghayoor H, Hoa SV, Hojjati M (2015) Multi-objective design optimization of variable stiffness composite cylinders. Comp Part B Eng 69:249–255. https://doi.org/10.1016/j.compositesb.2014.10.011
65. Schietzold FN, Graf W, Kaliske M (2021) Multi-objective optimization of tree trunk axes in glulam beam design considering fuzzy probability based random fields. ASCE-ASME Journal of Risk and Uncertainty in Engineering Systems Part B: Mechanical Engineering, 7(2). https://doi.org/10.1115/1.4050370
66. Schietzold FN, Heinzig S, Fina M, Graf W, Freitag S, Kaliske M (2024) Simulation of fuzzy probability based random fieldswith non-gaussian marginal distributionsby efficient nataf transformation method. In: ESREL 2024 collection of extended abstracts, 23–27 June 2024 Cracow, Poland, Polish Safety and Reliability Association
67. Schietzold FN, Leichsenring F, Götz M, Graf W, Kaliske M (2021) Robustness versus performance—nested inherence of objectives in optimization with polymorphic uncertain parameters. Adv Eng Softw, 156. https://doi.org/10.1016/j.advengsoft.2020.102932
68. Schietzold FN, Schmidt A, Dannert MM, Fau A, Fleury RMN, Graf W, Kaliske M, Könke C, Lahmer T, Nackenhorst U (2019) Development of fuzzy probability based random fields for the numerical structural design. GAMM-Mitteilungen 42(1):e201900004. https://doi.org/10.1002/gamm.201900004
69. Schweizer M, Fina M, Wagner W, Kasic S, Freitag S (2024) Uncertain pedestrian load modeling for structural vibration assessment in footbridge design. Eng Struct 311:118070. https://doi.org/10.1016/j.engstruct.2024.118070
70. Sofi A, Romeo E, Barrera O, Cocks A (2019) An interval finite element method for the analysis of structures with spatially varying uncertainties. Adv Eng Softw 128:1–19. https://doi.org/10.1016/j.advengsoft.2018.11.001
71. Sudret B, Der Kiureghian A (2000) Stochastic finite element methods and reliability—a state-of-the-art report
72. Tatting BF (1998) Analysis and Design of variable stiffness composite cylinders. PhD thesis, Faculty of the Virginia Polytechnic Institute and State University
73. Taylor RL (2024) Finite element analysis program (FEAP). http://www.ce.berkeley.edu/projects/feap/
74. Vanmarcke E (2010) Random fields: analysis and Synthesis. World Scientific, Singapore
75. Wagner HNR, Hühne C, Elishakoff I (2020) Probabilistic and deterministic lower-bound design benchmarks for cylindrical shells under axial compression. Thin Walled Struct 146:106451. https://doi.org/10.1016/j.tws.2019.106451
76. Wagner W (1995) A note on FEM buckling analysis. Commun Numer Methods Eng 11(2):149–158. https://doi.org/10.1002/cnm.1640110208
77. Wagner W, Gruttmann F (2005) A robust non-linear mixed hybrid quadrilateral shell element. Int J Numer Methods Eng 64(5):635–666. https://doi.org/10.1002/nme.1387
78. Wagner W, Wriggers P (1988) A simple method for the calculation of postcritical branches. Eng Comput 5(2):103–109. https://doi.org/10.1108/eb023727
79. Wang Z, Almeida JHS Jr, St-Pierre L, Wang Z, Castro SGP (2020) Reliability-based buckling optimization with an accelerated kriging metamodel for filament-wound variable angle tow composite cylinders. Comp Struct 254:112821. https://doi.org/10.1016/j.compstruct.2020.112821
80. Wang Z, Wan Z, Groh RMJ, Wang X (2021) Aeroelastic and local buckling optimisation of a variable-angle-tow composite wingbox structure. Comp Struct 258:113201. https://doi.org/10.1016/j.compstruct.2020.113201
81. Weber P, Fina M, Wagner W (2019) Time domain simulation of earthquake exitited buildings using a fuzzy stochastic approach. In: Beer M, Zio E (eds) Proceedings of the 29th European safety and reliability conference (ESREL), 22–26 Sept 2019, Hannover, Germany. https://doi.org/10.3850/978-981-11-2724-3_0155-cd
82. White SC, Weaver PM (2016) Towards imperfection insensitive buckling response of shell structures-shells with plate-like post-buckled responses. Aeronaut J 120(1224):233–253. https://doi.org/10.1017/aer.2015.14
83. White SC, Weaver PM, Wu KC (2015) Post-buckling analyses of variable-stiffness composite cylinders in axial compression. Comp Struct 123:190–203. https://doi.org/10.1016/j.compstruct.2014.12.013
84. Wu K, Gürdal Z (2012) Thermal testing of tow-placed, variable stiffness panels. In: 19th AIAA applied aerodynamics conference. https://doi.org/10.2514/6.2001-1190
85. Zhou X-Y, Gosling PD (2018) Towards an understanding of variations in the buckling of tailored variable angle tow composite plates. Comp Struct 203:797–809. https://doi.org/10.1016/j.compstruct.2018.07.061